

# Optical coherence tomography in biomedical research

Julia Walther · Maria Gaertner · Peter Cimalla ·  
Anke Burkhardt · Lars Kirsten · Sven Meissner ·  
Edmund Koch

Received: 1 April 2011 / Revised: 19 April 2011 / Accepted: 21 April 2011 / Published online: 12 May 2011  
© Springer-Verlag 2011

**Abstract** Optical coherence tomography (OCT) is a non-invasive, high-resolution, interferometric imaging modality using near-infrared light to acquire cross-sections and three-dimensional images of the subsurface microstructure of biological specimens. Because of rapid improvement of the acquisition speed and axial resolution of OCT over recent years, OCT is becoming increasingly attractive for applications in biomedical research. Therefore, OCT is no longer used solely for structural investigations of biological samples but also for functional examination, making it potentially useful in bioanalytical science. The combination of in vivo structural and functional findings makes it possible to obtain thorough knowledge on basic physiological and pathological processes. Advanced applications, for example, optical biopsy in visceral cavities, have been enabled by combining OCT with established imaging modalities. This report gives an outline of the state of the art and novel trends of innovative OCT approaches in biomedical research in which the main focus is on applications in fundamental research and pre-clinical utilization.

**Keywords** Optical coherence tomography · Instrumentation · Application · Biomedical imaging

## Introduction

Optical coherence tomography (OCT) is a particularly successful story of a new technology arising in the early 90s. Although based on the versatile Michelson interferometer [1], the term “optical coherence tomography” was coined in the famous work of Huang and Fujimoto in 1991 [2]. Based on the database PubMed for biomedical literature, the number of publications with the term “optical coherence tomography” in the title increased slowly until 2002, whereas an almost linear increase in the number of publications, with a steep slope of more than 200 per year can be found since then (Fig. 1). This increasing attractiveness of OCT is primarily ascribable to continual technical advances in the generation and detection of photons in the near-infrared wavelength range (NIR) and the growing demand for tomographic imaging systems in medical diagnosis and therapy planning. Figure 1 also confirms the rapid developments and improvements in technology and application of the OCT imaging technique in the last decade.

OCT can be described as a noninvasive, contactless, in vivo optical imaging technique which provides cross-sectional images of highly scattering subsurface samples, for example, biological tissue, with high axial resolution of 1–15  $\mu\text{m}$ . Technically, OCT is based on low-coherence interferometry of the backscattered light from within the sample to measure the magnitude and echo time delay and with it depth information about the investigated object. Viewed in a biological context, optical tomography, for example OCT, is enabled by the optical window, also known as the therapeutic or NIR window, in which biological tissue has less absorption and scattering in the NIR wavelength range, for which reason maximum penetration depth of light into tissue is achieved. Because

---

Julia Walther and Maria Gaertner contributed equally to this review

Published in the special issue *Biophotonics* with Guest Editors Jürgen Popp and Reiner Salzer.

---

J. Walther · M. Gaertner · P. Cimalla · A. Burkhardt · L. Kirsten ·  
S. Meissner · E. Koch (✉)  
Dresden University of Technology, Faculty of Medicine Carl  
Gustav Carus, Clinical Sensing and Monitoring,  
Fetscherstrasse 74,  
01307 Dresden, Germany  
e-mail: edmund.koch@tu-dresden.de

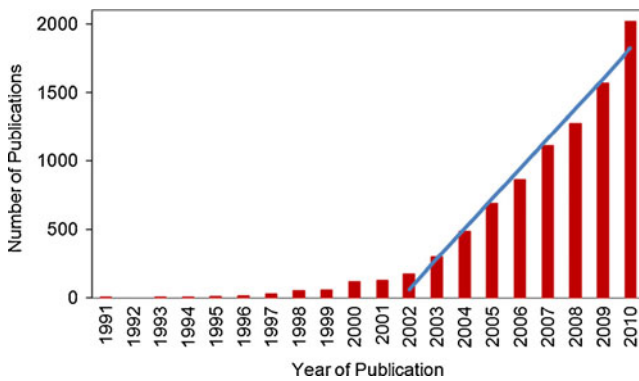


**Fig. 1** Number of publications in PubMed containing “optical coherence tomography” as a function of year (date, February 21, 2011). A linear regression between 2002 and 2010 yields a slope of more than 200 publications per year

most of the incident photons are transmitted and absorbed, only a small part of ballistic and quasi-ballistic photons hold the image information, resulting in a maximum OCT imaging depth of approximately 2–3 mm. Because of the use of NIR, a first advantage of OCT is the minor radiation exposure compared with the other techniques of tomographic imaging, for example computer tomography (CT) and  $\mu$ CT. Clinically, the noninvasive application, the relatively low cost, the robustness, and the transportability of most OCT systems can be named as additional advantages. Furthermore, OCT, as an optical method, features high-resolution imaging which cannot be achieved by use of ultrasound (US), CT, and magnetic resonance tomography (MRT). In addition to these advantages, the main benefits of OCT, especially in biomedical research, are the contactless application and higher resolution compared with high-frequency US, and the large imaging depth and 3D imaging speed in comparison with conventional confocal microscopy.

Nowadays, many publications deal with technological improvements but a vast majority focuses on utilization of the method in a great variety of applications especially in biomedical research and clinical medicine [3]. Biomedical imaging using OCT comprises, in particular, the “optical biopsy” to enable in situ and in vivo visualization of biological tissue which is not achievable with conventional excisional biopsy for histopathology. Additionally, standard biopsy cannot be realized for several tissues, for example retinal microstructures in the eye. The research of Huang et al. [2] and work published before this by Fercher et al. [4] and Hitzengerger [5], had already focused on the imaging of the eye fundus, because the ocular structures are largely transparent and other methods fail to give high-resolution images. Today, OCT has become a standard technique for clinical imaging in ophthalmology. Another clinically promising application is OCT imaging in hollow organs and cavities, e.g. the esophagus [6, 7] and human vessels

[8]. In biomedical research, the backscattered light not only furnishes information on amplitude and phase but also physical quantities, for example state of polarization and optical frequency shift which can be used for functional imaging. OCT thus facilitates visualization and quantification of physiological data, by analyzing the backscattered light, in addition to directly available structural information. Accordingly, the properties of tissues can be determined more precisely, for instance birefringence by polarization-sensitive OCT, blood flow velocities by Doppler OCT, and blood oxygenation saturation by spectroscopic OCT.

This article is an overview of basic principles, technological advances, and selectively established but also upcoming applications of OCT. This review summarizes the state of the art and future developments in OCT as an emerging imaging technique in biophotonics with the intention of revealing OCT as a new tool for researchers in analytical and bioanalytical science. In the next section, basic concepts of OCT system setups are reviewed. Subsequently, general and some specific applications of OCT in fundamental biomedical and pre-clinical research, subdivided into structural and functional OCT imaging, are presented without the objective of completeness. The final section of this review is a short summary of and outlook on the powerful imaging technique OCT.

## Concepts and instrumentation of OCT

### General

In general, OCT is based on white light interferometry in which the information carried by the interference signal is used to obtain the amplitude of the back reflection as a function of sample depth. Because OCT is an interferometric method, it is sensitive to the amplitude of the signal, enabling very small signals to be detected. The sensitivity of OCT systems is specified by the minimum reflection of a plane surface that gives a signal equivalent to the noise, referred to as the signal-to-noise ratio (SNR), reaching values of more than 100 dB. It is, therefore, possible to detect a signal from a sample structure reflecting  $10^{-10}$  of the incident light.

A huge quantity of technological concepts for performing OCT has been proposed during the past 20 years [2]. OCT systems can be realized using bulk optics but the flexibility and the large variety of available fiber optic components favors designs using monomode fibers. The classical layout of an OCT system is based on the Michelson interferometer, in which the fiber optic variant consists of a  $2 \times 2$  fiber coupler with the reference and the sample beam in the two arms opposite to those of the light source and detection (Fig. 2). If the setup contains

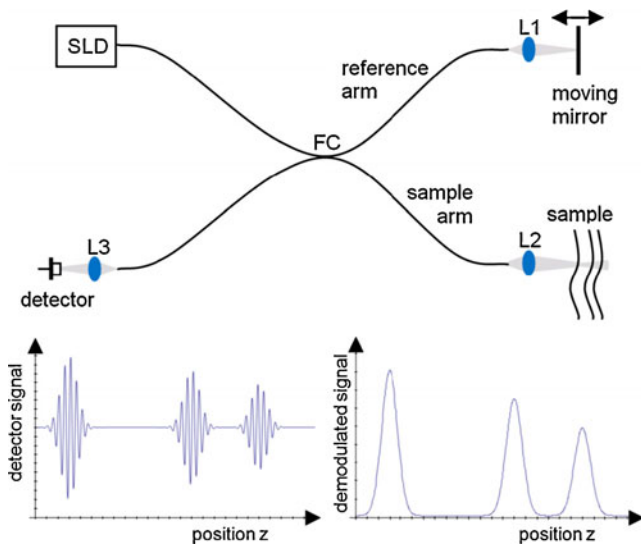


**Fig. 2** Schematic diagram of a time domain OCT system. The light from an SLD is split into sample and reference arm by a fiber coupler (FC). While the beam is reflected by a moving mirror in the reference arm, in the sample arm part of the light will be reflected from different structures of the sample. The interfering light is focused on a detector.  $L1$ – $L3$  are different lenses or objectives focusing the beam. Each reflection from the sample results in a burst of the detector signal at the corresponding position, which is demodulated by the electronics

conventional fibers, introducing an arbitrary amount of birefringence, polarization controllers in at least one arm of the interferometer are required to achieve a high interference contrast.

The wavelength range used for OCT has to be chosen in a way that guarantees high penetration into the specimen. Biological tissue has relatively high transmission in the range 700 to 1400 nm, where the lower limit is mainly a consequence of scattering and absorption of the chromophores hemoglobin and melanin and the upper limit is caused by the absorption of water. Concerning image quality, enhanced penetration depth is observed for wavelengths in the region of 1300 nm, because of less tissue scattering, whereas imaging at shorter wavelengths, in the region of 800 nm, enables higher resolution. In recent years, there has been increasing interest in wavelengths in the region of 1050 nm, because of the lower attenuation [9, 10]. To achieve a high axial resolution, the coherence length  $l_c$  of the light source has to be as small as possible. For a Gaussian shaped spectrum of width  $\Delta\lambda$  (FWHM) with a center wavelength  $\lambda_0$ ,  $l_c$  is given by Eq. (1):

$$l_c = \frac{2 \ln 2}{\pi} \cdot \frac{\lambda_0^2}{\Delta\lambda} \quad (1)$$

Although there are other definitions of the coherence length differing in the prefactor, this definition is used in the OCT literature because it provides the axial resolution directly. The large bandwidth of some light sources, in

conjunction with the fact that the resolution of OCT in a medium of refractive index  $n$  is  $l_c/n$ , enables resolution in tissue of approximately 1  $\mu\text{m}$  [11]. Although systems based on femtosecond lasers may achieve higher resolution, super luminescent diodes (SLD) are the better choice in respect of size, price, and ease of operation [12]. The spectral width of single SLDs, which is in the range 25 to 75 nm, enables axial resolution well below 10  $\mu\text{m}$  at wavelengths in the 800 nm region and approximately 10  $\mu\text{m}$  at wavelengths in the 1300 nm region. In recent years, supercontinuum light sources delivering radiation between 450 nm and 2  $\mu\text{m}$  have also been used for OCT applications [13]. The large spectral width enables the use of both bands in a single instrument [14, 15]. With regard to the remaining OCT system components, wavelengths in the region of 800 nm have the advantage that silicon can be used as a detector element, whereas fiber optic elements for telecommunication applications are available for wavelengths in the region of 1300 nm. In the following sections, the two different technical approaches used to acquire depth scans in OCT are explained.

#### Time-domain OCT

The first generation of OCT systems, denoted “time-domain OCT” (TD OCT), use a broadband light source and a single detector at the output of the interferometer; a fiber optic variant is shown in Fig. 2. By changing the length of the reference beam, the light backscattered from within the sample is analyzed in respect to the optical pathway. Because interference of a broadband wavelength spectrum is only detected when both arms of the interferometer have a difference in length shorter than the coherence length  $l_c$  of the light source, the origin of the back-reflected sample light can be determined accurately. By varying the length of the reference arm in a sawtooth or triangular manner and recording the oscillating signal, a depth scan is performed.

A single processed plot showing the amplitude of the backscattered signal at one point of the sample surface as a function of depth is called an A-scan, by analogy with ultrasonography. Moving the beam laterally relative to the sample in one dimension in order to obtain a cross-sectional view and coding the signal strength to the brightness in the resulting image is referred to as a B-scan. To obtain volumetric information about the sample, the beam is deflected in two dimensions relative to the sample surface. Scanning can be achieved by moving the sample, although deflection of the beam with one or two galvanometer scanners is preferred for high-speed imaging. The 2D and 3D information for generating B-scans or volume scans can also be acquired by illuminating a larger area of the sample and mapping the interference light onto a line or array detector, respectively. Systems using an array detector

acquire the image plane by plane, perpendicular to the direction of the illuminating light, resulting in a series of en-face images. Unfortunately, these systems suffer from the small quantum well capacity of the detectors, resulting in reduced dynamic range, and are more sensitive to sample motion because of the lower scan rate. Additionally, the transverse resolution of these systems may degrade because of multiple scattering within the sample and loss of the confocal advantage. The major advantage of TD OCT is that the focus position of the imaging system can be synchronously adjusted with the length of the reference arm, yielding very high transverse resolution over the total depth range [16]. Because the optical path in tissue is  $n \times d$ , where  $d$  is the depth in the tissue, and the focus position changes with  $d/n$ , the scan velocities must be adapted by  $n^2$ . For tissue with  $n$  of approximately 1.4, the scan velocities differ by a factor of almost two, which can be accomplished by placing the focusing optics of the sample arm and a folding mirror for the reference arm on the same translation stage [17]. Although such TD OCT systems achieve a very high resolution in all dimensions and have an almost unlimited ratio of measurement depth to resolution, they are limited in imaging speed (A-scans per time) by the mechanical movement of the translation stage [18]. To overcome these restrictions, various attempts have been made to reduce the accelerations, by using inter-reflection between two mirrors, for instance. The highest TD OCT imaging speed was achieved by introducing rapid scanning optical delay (RSOD) lines based on resonant galvanometer scanners with A-scan rates of a few kHz [19]. Many of these systems use gratings to separate the change in optical path from the phase delay to reduce the frequency of the interfering signal [20].

#### Fourier domain OCT

Despite all efforts to increase the speed of optical delay lines in TD OCT, the breakthrough in high-speed OCT imaging was achieved by introducing the concept of Fourier domain OCT (FD OCT) which is also known as “spectral interferometry” [21], “coherence radar”, or “spectral radar” [22, 23]. FD OCT is based on the fact that each wavelength of the light in the Michelson interferometer will interfere even if the reference and sample arms have totally different lengths. For a fixed difference in length between both arms, the interfering light will oscillate as a function of the wave number with a frequency that is proportional to the length difference. Therefore, Fourier transformation of the spectrum yields the backscattering amplitude as a function of depth. Generally, the interference spectrum is acquired in two ways, first by analyzing the interfering signal with a spectrometer which is referred to as spectral domain OCT (SD OCT), or, second, by sweeping the

wavelength of the light directed to the interferometer as a function of time. The latter is denoted as swept source OCT or optical frequency domain imaging (OFDI). The imaging speed of FD OCT systems is only limited by the readout rate of the line-scan camera of the spectrometer or the tuning velocity of the laser. Compared with TD OCT, the SNR achievable in the same time with the same amount of light is larger by a factor scaling with the square root of the number of depth data to be acquired [24–26]. Today, spectrometer-based OCT systems achieve velocities of more than 200,000 A-scans per second. By introducing new concepts of swept sources, OFDI systems have acquired even more than 20 million A-scans per second [27]. The basics of the different FD OCT concepts will be explained in the section below.

#### Spectral domain OCT

SD OCT uses a setup similar to that of TD OCT with the difference that the length of the reference arm is kept constant and the fourth arm of the interferometer contains a spectrometer, instead of a single photodetector, to resolve the interference pattern. The fiber-based principle of a typical implementation is shown in Fig. 3. Although this configuration enables high flexibility with regard to insertion of additional components in the reference arm for dispersion compensation [28] or phase shifting [29], the phase stability of systems having the interferometer in one

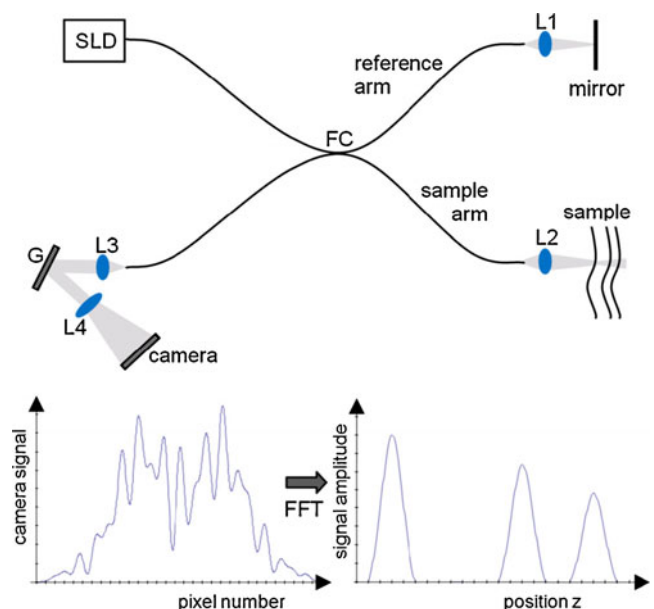


**Fig. 3** Schematic diagram of an SD OCT system. Different from TD OCT, the mirror in the reference arm is stationary. The interfering light from the fiber coupler (FC) is spectrally resolved by the grating (G) and focused on the line-scan camera. L1–L4 are different lenses or objectives. The camera detects the interference spectrum. After Fourier transformation the depth dependent signal is recovered



arm of the fiber coupler and leaving the second arm open is superior. Systems in which the sample and reference beam travel through the same fiber to the sample, are known as common path OCT [30–32]. Such a configuration enables the scanner head, containing the interferometer and the beam steering optics, to be placed in any position relative to the sample without any readjustment; this is especially favorable in biomedical applications in which a flexible point of view of the specimen is desired. Considering the detection arm, the beam must be expanded to an adequate width on the diffraction grating to achieve sufficient spectrometer resolution. The resulting dispersed beam is subsequently focused on the line detector of the spectrometer. Each readout of the CMOS or CCD line detector provides the information for a single A-scan. Therefore, the readout interference spectrum is corrected for background, then spectrally shaped [33], and afterwards transformed to be equidistant in wave number. Although transformation from wavelength to wave number can be achieved by simple interpolation [34], superior results in shorter computing time have been achieved by more sophisticated methods [35]. Generally, the transformation can be avoided using a combination of a grating and a prism, sometimes called “grism” [36, 37], resulting in a spectrometer which is linear in wave number. Fast Fourier transformation of the linearized data results in the backscattering amplitude of the sample as a function of depth (A-scan).

The axial resolution of FD OCT depends on the width and shape of the acquired interference spectrum. In SD OCT, the ratio between measurement range and resolution is limited by the number of detector elements,  $N$ . For the spectral shape of a Hanning window [38], which results in a good side lobe suppression, the ratio is given by  $N/4$ . Although line-scan cameras with approximately 10,000 elements are available [39], today's fast line-scan cameras with 1024 or 2048 elements limit this ratio to 256 or 512. Because of the width of the detector elements, crosstalk between neighboring elements, finite resolution of the spectrometer optics, and the interpolation procedure, the sensitivity is degraded at high spatial frequencies. This leads to a sensitivity drop-off between 10 to 20 dB at the end of the measurement range [40].

#### Optical frequency domain imaging (OFDI)

The alternative approach to SD OCT systems is the use of a light source tunable over a sufficient wavelength range in time comparable with the readout rate of the line-scan cameras in SD OCT systems. In OFDI, the spectral resolution is shifted from the end of the interferometer to the entrance (Fig. 4) so that the resulting interference spectrum is acquired time-resolved compared with the space-encoding in SD OCT. Despite some differences in

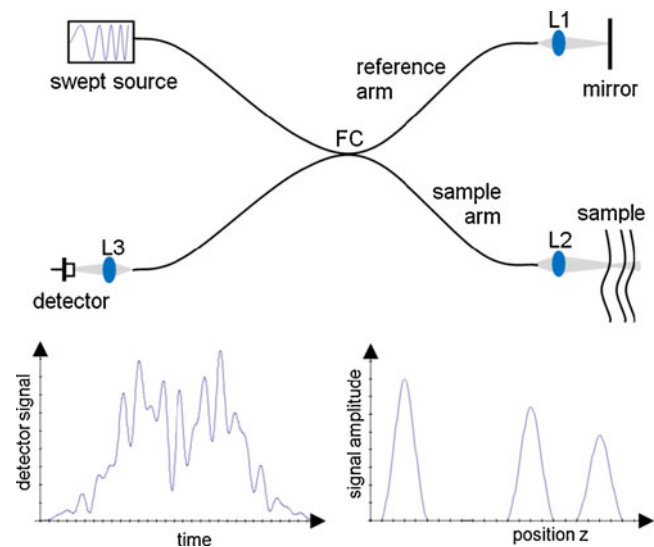


**Fig. 4** Schematic diagram of an OFDI system. Light from a fast tunable light source (*swept source*) is split into sample and reference arm by the fiber coupler (FC). The back-reflected light interferes at the fiber coupler and is sent to a single detector element. L1–L3 are different lenses or objectives. The detector signal is captured as a function of time. The time-dependent data are Fourier transformed to recover the depth-resolved signal

respect to the effect of sample movement, signal drop-off and other characteristics [41–43], SD OCT and OFDI systems are based on similar data processing. OFDI is especially interesting for the wavelength range above 900 nm where, so far, only a few fast line-scan cameras are available at a much higher price than silicon-based cameras of comparable speed.

In principle, wavelength tuning in swept source lasers is achieved by inserting a prism or grating in conjunction with a polygon scanner into the laser resonator [44]. As these designs are comparatively bulky, several implementations using a piezoelectric or MEMS-based tunable filter have been developed in recent years [45]. To reduce the effect of the relative intensity noise (RIN) of the laser source, the signal from the second arm of the interferometer or a part of the laser power is coupled to a second detector, in order to use differential detection techniques and by this means increase the SNR.

The repetition frequency of swept sources is limited by the maximum frequency of the tuning element and by the round trip time of the wave in the resonator, ensuring a monochromatic output of the laser; it is currently less than 100 kHz. To eliminate this limitation, Huber et al. [46] suggested a ring laser with a tuning element inside the long cavity where the roundtrip time is identical with the oscillation period of the tuning element. With this concept of Fourier domain mode locking (FDML) and accessory buffering techniques [27], there seems to be no speed limit for OCT other than the speed of electronics and the loss of

SNR resulting from the limited number of photons emitted in a single sweep. To achieve high SNR values, the operating conditions of FDML have to be chosen quite accurately [47]. Although, there is still room for improvement of OCT systems, with these concepts, a good basis for application of OCT in fundamental biomedical and preclinical research is provided; this will be the subject of the next section.

## Applications of OCT

OCT contains two fundamental features in biomedical studies: structural imaging and functional analysis. Considering the emerging increase of biophysical approaches and the ambition of quantitative characterization within the life sciences, OCT is an effective tool for comprehensive investigations. As an optical technique, OCT benefits from a simple and flexible design, facilitating exchanges and upgrades. Furthermore, it is possible to combine it with already established solutions, as found, for instance, in endoscopic imaging, to extend the field of applications of OCT to areas difficult to access. Limitations set by the unspecific backscattering of tissue can be overcome by integration of supplemental investigative tools, for example additional spectral bands, fluorescence imaging utilities, or polarization-sensitive optics. Focusing on some selected research areas, the next sections will give insight into several applications and recent developments of these methods and discuss their benefits for future research.

### Structural OCT

#### *Ophthalmic imaging*

The human retina was one of the first samples to be investigated by OCT, because ocular media are sufficiently transparent to enable easy optical access to the eye fundus. OCT enables *in vivo* cross-sectional visualization of retinal microstructure that cannot be obtained by any other noninvasive means of imaging [48]. Therefore, clinical application of OCT has mostly been developed in ophthalmology for diagnosis, staging, and monitoring of ocular diseases. Today several commercial ophthalmic OCT devices are available which use high-speed spectral domain detection. All instruments have comparable performance with an axial resolution of 4–6  $\mu\text{m}$  operating in the 800 nm wavelength region with imaging speeds of 25,000–40,000 axial scans per second [49] which enables real-time cross-sectional imaging.

As an alternative or extension to conventional ophthalmic imaging at 800 nm, OCT systems for research at

1050 nm have also been demonstrated. Because of less absorption of the retinal pigment epithelium and reduced tissue scattering on the one hand, and still sufficiently low light absorption by the aqueous ocular media in front of the retina on the other hand, this spectral range enables depth-enhanced visualization of the choroid [10, 50] and improved visibility of the retina in patients with opaque ocular media, for example cataracts [9].

One particular feature of OCT is that axial resolution is decoupled from transverse or lateral resolution. The axial resolution is mainly given by the coherence length of the applied light source whereas the lateral resolution is defined by the numerical aperture of the focusing optics, i.e. the beam diameter and the focal length, as in conventional microscopy. In ophthalmic imaging, the eye's cornea and lens are used as the imaging objective. Therefore, the lateral resolution is limited by the pupil size and the focal length of the eye and, in practice, even further reduced by ocular aberrations. To overcome this practical limitation, adaptive optics—well known in astronomy—is used in OCT systems for research to correct ocular aberrations. This instrumentation measures the wavefront distortion caused by the ocular media and corrects it by means of deformable mirrors or liquid crystal phase modulators. It has been shown that adaptive optics can significantly improve lateral resolution to 2–3  $\mu\text{m}$  compared with 15–20  $\mu\text{m}$  in conventional ophthalmic OCT [51]. Furthermore, adaptive optics increases imaging sensitivity especially at the photoreceptor layer and reveals single signal-rich structures located at the inner/outer photoreceptor segment junction and the posterior tips of the outer photoreceptor segment which are believed to represent individual cone cells [52, 53]. The conjunction of high axial resolution OCT with aberration-correcting adaptive optics is therefore often referred to as cellular imaging of the living human retina.

To understand the mechanisms underlying ocular diseases such as retinal degeneration, rodent models play a key role. It has been shown that OCT is also a suitable noninvasive measurement tool for monitoring retinal degeneration in small laboratory animals, for example mice [54] and rats [55]. Although, imaging in the 800 nm wavelength region is preferred [56–58], as in humans, OCT of the rodent retina is also reported at 1060 nm [59] and 1300 nm [60]. It has been shown that there is a good correlation between OCT data and histology, so OCT is a valuable tool for analysis and monitoring of structural changes in the retina for noninvasive time-course studies in animal models [58]. Figure 5 shows typical high-resolution rodent retinal OCT imaging in the 800 nm wavelength region which was applied in an *in vivo* RCS (Royal College of Surgeons) rat model with degenerated photoreceptor layer and outer nuclear layer.

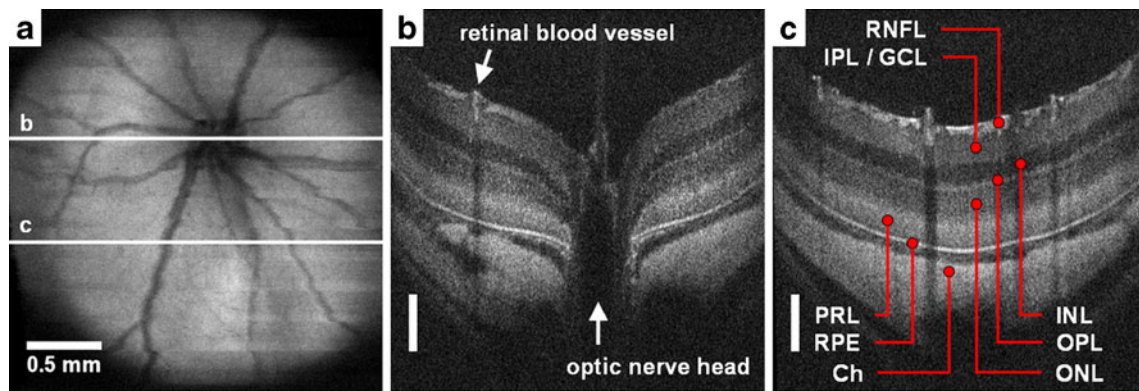


**Fig. 5** Noninvasive high-resolution OCT imaging of the retina in an in vivo RCS (Royal College of Surgeons) rat model with degenerated photoreceptor layer and outer nuclear layer, acquired in the 800 nm wavelength region. OCT fundus image (**a**) and two representative OCT cross-sectional scans at (**b**) and away from (**c**) the optic nerve head. The layered retinal microstructure consists of the retinal nerve

fiber layer (*RNFL*), inner plexiform/ganglion cell layer (*IPL/GCL*), inner nuclear layer (*INL*), outer plexiform layer (*OPL*), outer nuclear layer (*ONL*), photoreceptor layer (*PRL*), retinal pigment epithelium (*RPE*), and choroid (*Ch*). The vertical bars represent 100  $\mu\text{m}$  in the axial direction

In human retinal imaging, the collimated sample beam is conventionally relay-imaged on to the pupil by means of a lens pair and focused on to the fundus by the eye itself; this was also applied for retinal imaging in mice and rats [56, 57]. However, it is reasoned by others that this method is not optimum for small rodents, because the small size and short focal length of the eye imply a high numerical aperture objective lens design to cover a large measurement area on the retina. In addition, the short focal length of the eye increases optical aberration which degrades the OCT signal and reduces image quality. Alternatively, a contact lens made from a microscope coverslip and hydroxypropyl methylcellulose is used; this effectively removes the refractive power of the air–cornea boundary and enables the sample beam to be focused directly on to the rodent retina. Because of the corresponding enlargement of the eye's focal length, lower numerical aperture lens designs can be used to cover a sufficient measurement area on the retina. Furthermore, this technique reduces corneal aberrations and prevents the eye from dehydration [61, 62]. In general, it is also possible to image the entire mouse eye from the cornea to the retina in one OCT scan [63, 64], because of its small size. This enables noninvasive quantitative assessment of biometric ocular data such as intraocular distances and interface shapes of the ocular media, which is of interest in research on eye development. The structural tissue information delivered by ophthalmic OCT is a useful tool to study ocular pathology, for example age-related macular degeneration, diabetic retinopathy, and glaucoma, in animal models [48], to determine disease progression and treatment response. Beyond that, most recent advances tend toward combining high-resolution OCT with electroretinography (ERG) for simultaneous structural and functional monitoring of the retina in the rodent eye [65].

### Pulmonary imaging

The main advantage of OCT is its high spatial resolution and high imaging speed which make it suitable for study of biological tissue, for example lung parenchyma, with the objective of acquiring more knowledge of alveolar mechanics and dynamics. Prevalent imaging techniques are limited by spatial resolution, penetration depth into tissue, the possibility of dynamic 3D imaging, and the in vivo implementation which is desirable for imaging alveolar structures. The established technique is intravital microscopy (IVM) which is high-resolution and furnishes real-time images of pulmonary alveoli but no 3D information [66]. The low resolution limits computer tomography (CT) [67] and hyperpolarized  $^3\text{He}$  magnetic resonance imaging to acquire alveoli with diameters of approximately 100  $\mu\text{m}$  [68].  $\mu\text{CT}$  has sufficient resolution to image alveolar structures in fixed and stained tissue but, nevertheless, the high radiation and acquisition time required limit this technique for dynamic in vivo investigations on the alveolar scale [69]. It was recently shown that OCT can close this gap to image subpleural alveoli dynamically [66], three-dimensionally [70], in vivo [71], and with high resolution. Popp et al. and Meissner et al. used the model of an isolated perfused rabbit lung [72, 73] to investigate the correlation between pulmonary pressure and alveolar size. This model was chosen because of several advantages compared with in vivo models, for example minimization of motion artifacts caused by the heart beat and the cyclic ventilation. Furthermore, it enables unlimited access to the lung tissue and application of a constant positive airway pressure (CPAP) for longer periods of time to set stable conditions for OCT imaging. By combining OCT and IVM, it can be ensured that identical alveolar structure in all OCT images at different CPAP levels is acquired. Analysis of the

alveolar changes with increasing CPAP results in an increase in alveolar size with hysteresis behavior measured by OCT and IVM.

Mertens et al. [66] carried out OCT imaging of subpleural alveolar structures in an in vivo mouse model in which a transparent thorax window [74] was implemented to acquire images by OCT and IVM simultaneously. OCT imaging was triggered by the inspiratory plateau pressure, ensuring a regularly ventilated mouse during image acquisition. Three-dimensional OCT image stacks were taken at the inspiratory and the expiratory plateaus; the result of the inspiratory phase at 24 mbar is presented in Fig. 6a. A 3D reconstruction of the identical subpleural alveolar cluster taken at the inspiratory (gray) and expiratory (purple) plateaus is displayed in Fig. 6b. The relative change of the alveolar area in this in vivo model is comparable with results from isolated rabbit lungs [73].

A recent study has achieved quasi 4D (3D + time) in vivo imaging of murine lung parenchyma during the inspiratory phase by using high-speed swept source OCT [75] in combination with an intact chest [71]. With it, 3D real-time imaging of alveolar behavior during spontaneous breathing is enabled.

OCT has also been used to characterize the mechanical behavior of lung parenchyma by indentation experiments on the lobe surface of mammalian lungs. Silva et al. showed that ventilation with 100% oxygen significantly alters the mechanical behavior of the lung [76]. This technique allows statements of short-term effects less than a minute after inhalation of highly concentrated oxygen compared with the effects defined by symptoms occurring after hours of inhalation, or post mortem histology. By combining OCT and endoscopic technique (EOCT), it is possible to realize an in vivo optical biopsy of the upper airways and the thoracic cavity. Coxson et al. and Lam et al. used EOCT to investigate the thickness and structure of the bronchial wall and preinvasive internal lesions, highly spatially resolved and in 3D, which cannot be achieved by

use of established techniques, for example bronchoscopy or CT [77, 78]. New findings of the geometry and mechanical behavior of the alveolar structures and the upper airways achieved by use of OCT help to develop protective artificial ventilation, especially for patients with an acute lung disease, and optimize ventilation strategies to avoid ventilator-induced lung injury.

With regard to in vivo imaging of pleural-based malignancies, Xie et al. reported intrathoracic 3D imaging of suspicious lesions and tumors on the inner chest wall and lung surface in a rabbit model of pleural cancer, in vivo, by use of endoscopic swept source OCT [79]. In this technique, in vivo differentiation between normal tissue and tumor using 3D images, combining surface morphology and internal tomography, is enabled by EOCT under guidance of a visual thoracoscopic system. Because the most common type of cancer is lung cancer, the proposed combination of a digital video thoracoscope and an OCT endoscope is a basic technological development for early detection of abnormal lung tissue, leading to lung and other pleural cavity cancers, in the future. The potential of OCT for initial cancer imaging and diagnosis is presented in detail in the section “Cancer imaging”.

#### Endoscopic imaging

Endoscopic OCT (EOCT) enables micrometer-scale sub-surface in vivo imaging of biological tissue structures within tubular organs and cavities. To ensure a large imaging depth, most systems operate in the 1300 nm wavelength region. Types of endoscopy can be classified on the basis of the use of forward and side-imaging probes; the latter have been developed and applied for examination of tubular organs, for example the gastrointestinal (GI) tract, the vascular system, and the respiratory system. For side-imaging systems, the light is emitted and collected on the side of the endoscope by use of a prism [80] whereas forward-imaging systems

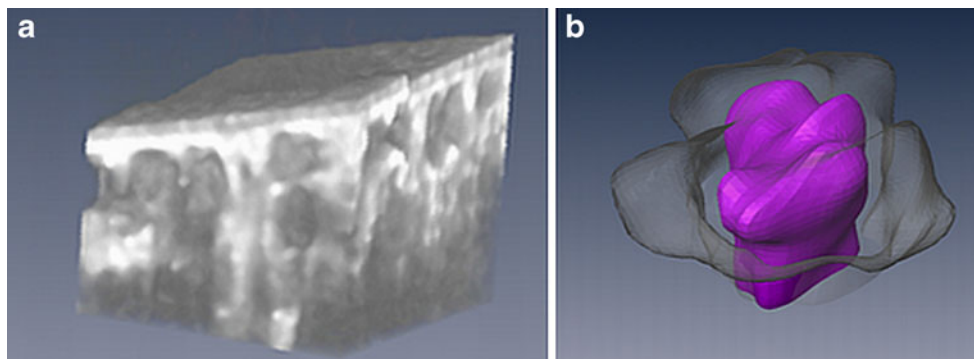


**Fig. 6** (a) Typical 3D OCT image ( $800\ \mu\text{m} \times 800\ \mu\text{m} \times 500\ \mu\text{m}$ ) of murine subpleural lung tissue acquired in vivo in the inspiratory plateau at a plateau pressure of 24 mbar. The *pleura visceralis* and

single alveoli can be seen. (b) 3D reconstruction of an alveolus acquired in the expiratory (purple) and inspiratory plateau (gray). An increase in volume and a change of shape are recognizable



emit and collect the light at the front; this is favored for image guidance during surgery, device replacement, and image-guided biopsy [81, 82]. Most EOCT devices are side-imaging probes whose generally flexible design, consisting of an optical fiber, a lens, e.g. a gradient index (GRIN) lens, and a prism to deflect the light sideways, enables construction of endoscopic probes with very small dimensions—up to 0.4 mm in diameter. Basically, side-imaging EOCT probes enable 2D depth-resolved imaging of subsurface tissue by rotating the optical system with the possibility of 3D imaging by back and forth translation of the catheter and endoscopic probe, respectively [83, 84]. Currently, the best specifications achieved by different side-imaging optical setups are lateral resolution of 8  $\mu\text{m}$ , axial resolution of 2.4  $\mu\text{m}$ , a working distance of 2.5 mm, and a circumferential field of view (FOV) [80, 85–87]. These particular optical characteristics are affected by each other and define the specific boundary conditions of the EOCT system. New side-imaging optical designs that achieve a very large working distance of approximately 9–12 mm while avoiding direct contact with the investigated tissue have recently been demonstrated [88, 89]. For forward-imaging probes, different optical designs for OCT imaging include, for example, a fiber-optics imaging bundle for flexible endoscopy and long GRIN relay lenses for rigid endoscopy. Enhancement of the rigid GRIN-lens-based EOCT probes using two angle-cut rotating GRIN lenses, also referred to as paired-angle rotation-scanning OCT (PARS OCT), enable scanning of the OCT sample beam across the forward region ahead of the EOCT probe tip over a wide FOV [90]. In comparison with side-imaging probes, forward-imaging endoscopes are relatively bulky—the smallest diameter so far mentioned in the literature is approximately 1.65 mm [90]. Considering the specifications of optical imaging, lateral resolution of  $\sim 10$   $\mu\text{m}$ , axial resolution of 9.3  $\mu\text{m}$ , a working distance of 7.5 mm, and a FOV of  $\sim 6$  mm are achievable by use of the different EOCT optics developed [90–92]. An advantage of forward over side-imaging probes is the directly available 3D imaging without implementation of an automated mechanical pullback device. Different approaches for 3D imaging have recently been proposed, e.g. 2D scanning at the proximal end of a fiber bundle or servo-mirror-based 2D beam scanning at the proximal side of a GRIN lens; some of the forward-imaging probes are, nevertheless, solely applicable for 2D imaging. Another promising design is the use of one or two-axis micro-electromechanical system (MEMS) mirrors at the distal end, enabling 2D or 3D imaging for both side- [93, 94] and forward-imaging EOCT.

The combination of OCT with the endoscopic technique has led to several areas of application not previously accessible. The main field of EOCT applications in

fundamental and clinical research is cancer staging in different mucosa of internal hollow organs to ensure the early detection of malignant lesions. EOCT was first applied to the GI tract for visualizing the layers of the esophageal wall [6, 82]. It has, moreover, been shown that OCT enables imaging of the esophageal submucosal and mucosal layers, enabling differentiation of Barrett's esophagus from normal esophageal mucosa, and therefore monitoring of the structurally changed tissue; this is essential for preventing the progression of esophageal carcinoma [95–97]. Recently, Hatta et al. [98] revealed that it is possible to assess the depth of tumor infiltration in superficial esophageal squamous cell carcinomas by determining the extent of destruction within the different layers of the esophageal wall, although it is still very difficult to distinguish between normal esophageal and diseased tissue.

Another important application of EOCT is in vivo monitoring of coronary artery disease, in which diagnosis of stenotic lesions at an early stage is essential to avoid the imminent artery occlusion [8, 83, 99]. Brezinski has shown that EOCT is a suitable method for imaging unstable coronary plaques, which can rupture in the case of a necrotic core and thin wall causing an acute coronary syndrome, combined with imaging of the stents subsequently deployed for elimination of the stenosis. Considering vascular imaging in combination with EOCT, Doppler OCT as a functional approach is used for detection of mucosal and submucosal microcirculation of tubular organs in which the different patterns of the capillary system of normal and diseased tissues is of interest for medical diagnosis. Current spatial and velocity resolution in EOCT enable the visualization of small subsurface blood vessels that could not previously be imaged [100, 101].

Another field of research, in which EOCT is of significant clinical interest, is the respiratory system. There is a range of pathological conditions, including bronchial inflammation and laryngeal carcinoma, one of the most common primary head and neck malignancies. Recently, an EOCT system was presented in which a long GRIN lens was attached to a laryngoscope for in vivo human imaging during a typical office-based laryngoscopy [102]. Generally, the use of EOCT in lung screening is still in its early stages, with the hope of early detection of bronchial inflammation and laryngeal cancer in the future [103]. The range of disease conditions that can potentially benefit from early and noninvasive diagnosis with EOCT-based imaging systems is wide and still not opened up in each area of application. For instance, early detection and diagnosis of lesions and changes in the morphology of the oral cavity, the bile duct, and the urinary and reproductive tract could profit from advances in EOCT-based imaging [104–107]. These investigations are still in the early stages and have promise for the future.

## Cancer imaging

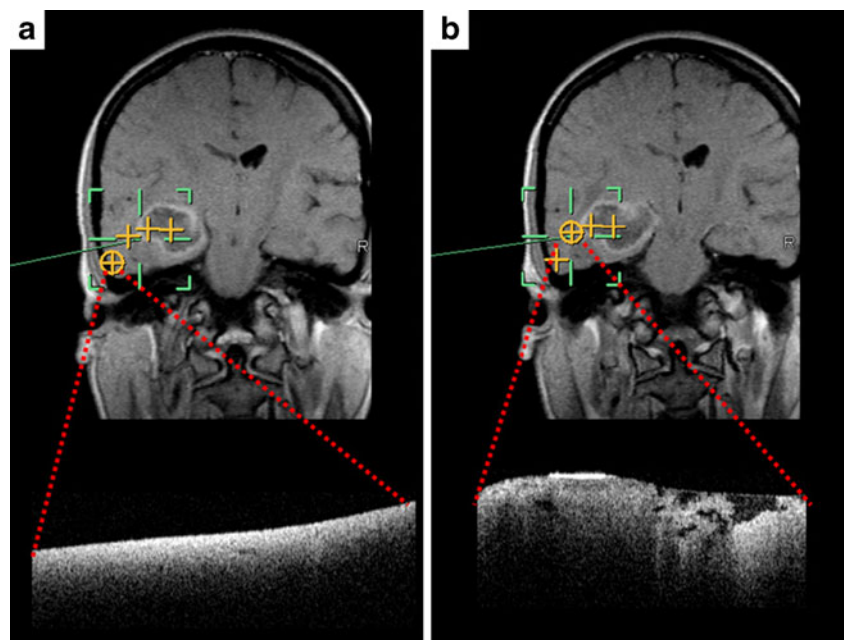
Among the fifteen leading causes of death in the United States in the year 2007, cancer was in second place, with 23.2%, closely behind heart diseases, with 25.4%. For pancreatic, lung and bronchial, esophageal, and gastrointestinal carcinoma, especially, survival is between 6 and 26% [108]. As a consequence, a major interest in pre-clinical research is early detection and classification of malignant tissue and the supply of means for noninvasive in vivo diagnosis and treatment.

Because endoscopic probes have the advantage of small size and a flexible adjustment to the sample at locations difficult to access, first studies used EOCT to investigate suspicious lesions in various internal hollow organs, for example the gastrointestinal and respiratory tracts [6], the bladder and urinary tract [109], and the esophagus [110]. Because of the optical nature of OCT, it can also be incorporated into well-established clinical tools, for example bronchoscopes [111] and laryngoscopes [112], for additional guidance and cancer staging.

Previous applications of OCT for cancer detection focused on structural characterization of suspicious lesions and comparison with histological findings as a substitute for conventional biopsy. Successful correspondence was found in vitro, for example, for human biopsies from patients suffering from transitional cell carcinoma in the bladder [109] and cervix, for which OCT revealed early cervical carcinoma on the basis of an irregular epithelial layer and thickening of the basement membrane [113]. OCT is also promising with regard to comparison of the

morphological structure of lymph nodes taken from a carcinogen-induced rat mammary tumor model and the corresponding histological results [114]. For in vitro human breast cancer studies, especially, OCT is extremely effective in recognizing highly-scattering tumor regions from normal nearly transparent adipose tissue structures, with high contrast resulting in improved identification ability [115, 116]. Similarly, EOCT for in vivo investigation of the esophagus is giving promising results in revealing endothelial abnormalities, for example highly reflective mucosa found for Barrett's esophagus and morphologic disorganization in esophageal adenocarcinoma [95]. Although these predominantly in vitro findings suggest great potential for early detection of progressing cancer in vivo, the imaging depth of OCT of merely 2 to 3 mm in biological tissue limits application to superficial tissue abnormalities. This drawback is negligible in intraoperative diagnosis by use of OCT to distinguish the boundary between normal and malignant regions during surgery [117–119]. Figure 7 shows an example of ex vivo OCT imaging applied to freshly excised human brain tissue revealing the transition from normal brain structures to tumor regions during resection. Besides the immediate analysis of tissue sections taken during surgical intervention, the OCT system used for this study can also be positioned above the resection cavity via a flexible arm attached to an operating table, providing additional guidance and control. A further example of OCT-guided surgery is the detection of human breast tumor margins as seen in Fig. 8. Strongly backscattering tissue regions, which are revealed by OCT images obtained during surgical intervention, correspond

**Fig. 7** Comparison of MRI images (*top*) and OCT (*bottom*) during resection of a large right temporal glioblastoma WHO grade IV tissue sample. Biopsies were taken from the marked regions indicated with yellow circles in the MRI images and were immediately subjected to OCT imaging. Correlation was achieved using a neuronavigation system (BrainLab, Heimstetten, Germany). Normal brain tissue (**a**) and the transition from normal to high contrast tumor areas (**b**) can clearly be recognized. (Courtesy of Alf Giese from the Department of Neurosurgery at the Georg-August-University of Göttingen; image reprinted from Ref. [117] with permission from Springer)



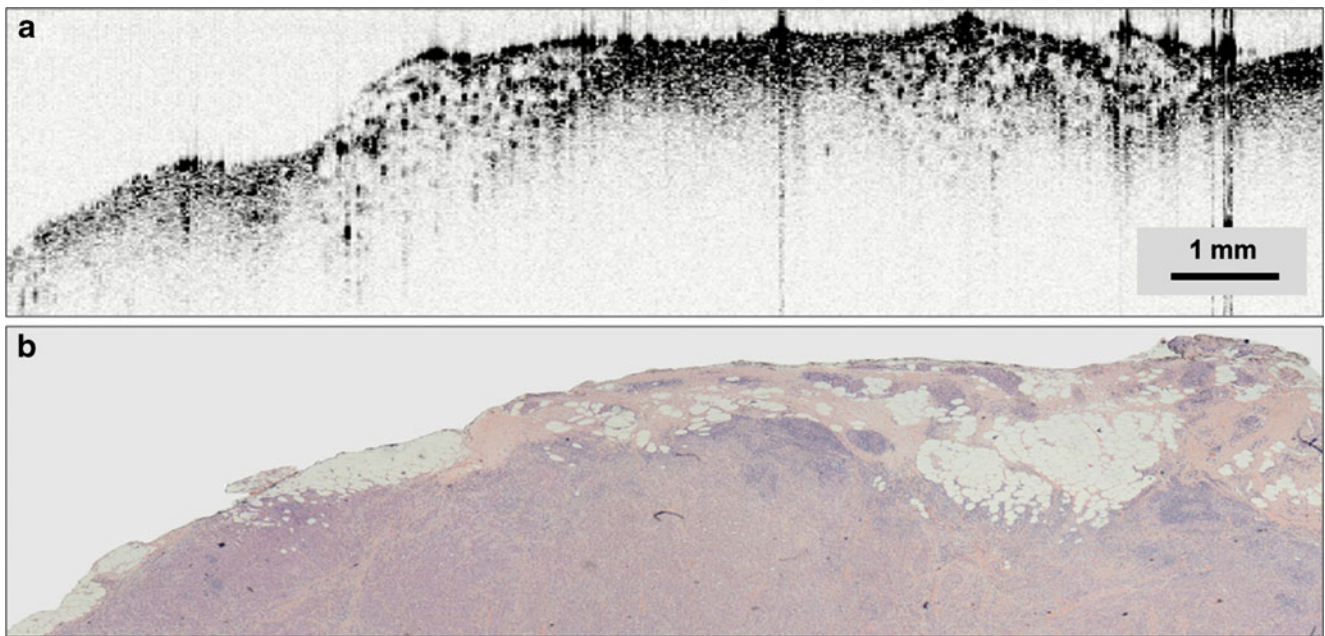


**Fig. 8** Intraoperative OCT (a) with post-operative histology correlation (b) of a positive surgical margin acquired during human breast cancer surgery. (Image courtesy of Stephen Boppart from the Beckman Institute at the University of Illinois at Urbana-Champaign)

well to the cancer structures visible in the post-operative histological analysis.

Despite a few successful in vitro and in vivo cancer studies, optical biopsy using OCT remains challenging, because of low resolution and unspecific imaging. Comparison with histological studies shows good agreement, but OCT still cannot serve as a stand-alone classification technique. Although changes in epithelial structure and thickness, and bright backscattering signals from tissue with high cell nucleus densities reveal abnormalities, early-stage characterization and differentiation between benign and malignant tumors is difficult to achieve simply on the basis of the structural information from OCT images [120]. Additional classification of cancer-specific structural details detected by OCT and performed by experienced pathologists would help to establish this technique as an in vivo adjunct to conventional biopsy. First attempts at more sensitive cancer detection implement comprehensive analysis of the interference signal for automatic tissue categorization [121]. Further approaches also use complementary information on the tumor microenvironment, for example angiography and lymphangiography [122]. In this case, phase variance analysis, based on the phase information of the interference signal as used for Doppler flow measurements (discussed in the section “[Doppler flow measurement](#)”), enables detection and segmentation of vessels located in the mouse brain in vivo. Further enhanced specificity and imaging contrast can also be achieved by binding conjugated gold nanoparticles to cancer cells; this has been shown by confocal reflectance microscopy of human cervical tissue and

would, indeed, probably also be suitable for OCT imaging [123]. Combination with complementary optical techniques, for example fluorescence lifetime imaging (discussed in the section “[Combination with complementary optical methods](#)”) may also increase specificity.

Use of OCT is feasible in pre-clinical cancer studies; widespread applications include in vitro and in vivo tissue characterization, early cancer detection at a nearly histological level, and intraoperative guiding systems. Because of its minimally invasive nature, OCT is an attractive tool for time-course studies, as found, for example, in investigation of tumor progression in mouse brain tissue [122], making it suitable for basic research applications. Specificity is achieved for some cancer types, for example breast cancer, in which the scattering difference between normal and tumor tissue is prominent. Epithelial abnormalities investigated in several studies of the gastrointestinal tract also reveal tissue characteristics specific to the underlying pathology, although this must still be supported by use of histological sections. For nearly homogeneous samples, for example the brain, additional functional imaging methods, for example angiography of the microenvironment, may lead to promising results for pre-cancer investigations in fundamental research and, especially, clinical implementation in the future.

#### *Vasodynamic imaging*

As discussed in previous sections, OCT enables contactless, noninvasive, high-resolution structural imaging which is



also beneficial for vasodynamic monitoring in an in vivo mouse model as a contribution to quantification of the pathogenesis of arteriosclerosis starting with increasing stiffness of the vessel wall [124]. The established technique for investigating the vasodynamics of vessels is isometric tension recording using isolated vessels ex vivo in micro vascular myography [125]. As new method for in vivo examination of vasodynamics of the murine *arteria saphena*, without preparation traumata and in the anatomical context with innervations of nerves and blood pressure, OCT has recently been introduced [126]. This in vivo mouse model and, especially, these vessels were chosen for fundamental arteriosclerotic research by OCT, because of their advantageous anatomical position and their distinctive response to vasoactive stimuli. A representative OCT cross-section of murine saphenous blood vessels and the surrounding tissue detected by simultaneous dual-band OCT imaging (discussed in the section “Dual-band and spectroscopic OCT”) is illustrated in Fig. 9a. The acquired B-scans of the vascular structure imaged at 800 nm and 1250 nm simultaneously are used to generate the compounded image by pixelwise averaging of the intensity values in order to reduce the speckle noise. In comparison with the initial vessel diameter under control conditions in Fig. 9a, the endpoint of the vessel response of the saphenous artery after vasoconstriction and vasodilation induced by dermal application of the corresponding vasoactive stimulus is presented in Fig. 9b, c in which the significant change of the artery’s diameter becomes apparent. An advantage is that time-resolved quantification of the diameter change during vasoconstriction and vasodilation provides information on the elastic properties of the vessel. In a first study, an age-dependent change of the dynamic ratio and relative wall thickness for mice aged 6 and 20 weeks was shown [126]. In a further study, Muller et al. revealed, by use of OCT, increased stiffness of the vessel wall after 14 weeks of a high-fat diet compared with normal diet [127].

The main advantage of the new examination method is that sacrificing of the laboratory animal is no longer

necessary for investigation of vasodynamics. Additionally, experiments can be carried out at multiple time points with the same animal, enabling the analysis of long-term changes of the vasculature in conjunction with, e.g., transgenic mouse strains and pharmaceutical effects. As depicted in Fig. 9, OCT with high spatial resolution allows more precise observation of the thickness of the smooth muscle layer shown by the dark ring structure in the arterial wall; this could be of interest for investigation of the effect of hypertension, an important elicitor of the progression of early arteriosclerotic changes, in future research.

## Functional OCT

### Doppler flow measurement

Nowadays, OCT structural imaging is being extended with functional studies of the visualization and quantification of the physiological characteristics of biological tissue, for example metabolism [128, 129], elastography [130, 131], and blood circulation [132–135]. To realize the latter, Doppler OCT or optical Doppler tomography (ODT) was proposed to measure blood flow velocities, initially by using TD OCT [132–135]. In this, the axial flow velocity component is extracted from the Doppler frequency shift of the detected interference fringe intensity modulations [136]. By considering the broadening of the Doppler spectrum, the so-called Doppler bandwidth, due to probe beam geometry, the transverse component of the flow velocity, can be calculated [137]. In FD OCT, the method widely used to measure flow velocities is called phase-resolved Doppler OCT, which is based on the linear relationship between the phase shift of sequentially acquired interference signals and axial flow velocity [138–143]. Because of the high phase stability of SD OCT systems, an advantage over OFDI [144], and the high SNR compared with TD OCT [24, 25], Doppler flow imaging is often performed in combination with SD OCT. A Doppler flow B-scan acquired by SD OCT is presented in Fig. 10 using, as example, an in vivo vasodynamic study by means of the murine *arteria* and

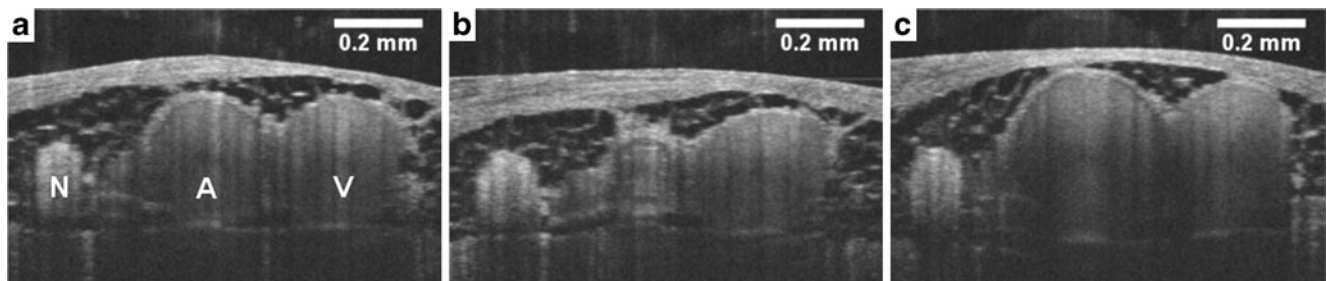


**Fig. 9** The image sequence shows typical results from a representative investigation of vasodynamics for (a) control condition, (b) vasoconstriction, and (c) vasodilation in the mouse model. The murine

*arteria saphena* (A), *vena saphena* (V) and *nervus vastus medialis* (N) can be seen



*vena saphena* (as discussed in the section “**Vasodynamic imaging**”).

Recently, different advances in Doppler FD OCT have been used for qualitative and quantitative flow velocity determination. For example, a modified Doppler algorithm called joint spectral and time domain optical coherence tomography (STdOCT) has been proposed for measurement of velocities of scattering parts with a low SNR [145] and was presented for 3D retinal and choroidal imaging of the human eye [146]. Another modified Doppler method for qualitative imaging of blood perfusion is 3D optical angiography (OAG) [29], which imposes a constant modulation frequency by moving the reference mirror during the A-scan acquisition to achieve separation between moving and static structures by a transverse Hilbert transform. An enhancement of OAG is the single-pass volumetric bidirectional blood flow imaging (SPFI) of Tao et al., by use of a modified Hilbert transform algorithm for introducing a constant Doppler frequency shift without the need for a moving reference arm [147]. This technique was enhanced by using a moving spatial frequency window to achieve velocity-resolved SPFI of several volumes within one 3D scan [148]. Similar to the 3D OAG by Wang et al., resonant Doppler flow imaging also generates a variable phase delay in the reference arm, by using an electro-optic phase modulator to enhance the backscattering signal of the moving structures [149]. This method relies only on the amplitude of the scattering signal and overcomes the signal power decrease arising from interference fringe blurring caused by sample motion [144]. The sample velocity is calculated by comparing the interference signal for the reference arm moving forward or backward with the signal when the reference arm is at rest.

Despite multifaceted enhancement of flow velocity detection by FD OCT, the most common and straightfor-

ward method for quantitative flow measurements with SD OCT is phase-resolved Doppler analysis. In this, the complex depth-encoded signal  $I(z)$ , processed by an inverse fast Fourier transform of the detected interference spectrum, contains both the amplitude  $A(z)$  and phase  $\phi(z)$  of the light reflected from the sample:

$$I(z) = A(z) \cdot e^{i\phi(z)} \quad (2)$$

where  $z$  corresponds to the optical length difference between reference and a particular backscattering sample layer. The OCT structural images are generated using  $A(z)$  and flow imaging is achieved by analyzing phase differences  $\Delta\phi(z)$  between points at the same depth in adjacent A-scans. To guarantee correlated speckle, and with this phases, at the compared depth points, at least two A-scans must be acquired at each transverse point [150]. Another way is to separate adjacent A-scans by a distance considerably less than the FWHM of the sample beam intensity profile; this can be achieved by oversampling in the transverse direction. The measurement geometry for the Doppler experiment is shown schematically in Fig. 11 by considering only one scattering particle with velocity  $\vec{v}$ .

The particle is detected in two consecutive A-scans at times  $T_1$  and  $T_2$ . The axial movement  $\Delta z$  during the integration time  $T_{A\text{-scan}} = (f_{A\text{-scan}})^{-1} = |T_1 - T_2|$  leads to a Doppler phase shift  $\Delta\phi(z)$  given by:

$$\Delta\phi(z) = \frac{4\pi n \cdot v_z T_{A\text{-scan}}}{\lambda} \quad (3)$$

where  $n$  represents the refractive index and  $v_z$  is the axial velocity component of the moving sample. With known Doppler angle  $\vartheta$  between the direction of the moving object and the horizontal, the absolute sample velocity  $v$  can be

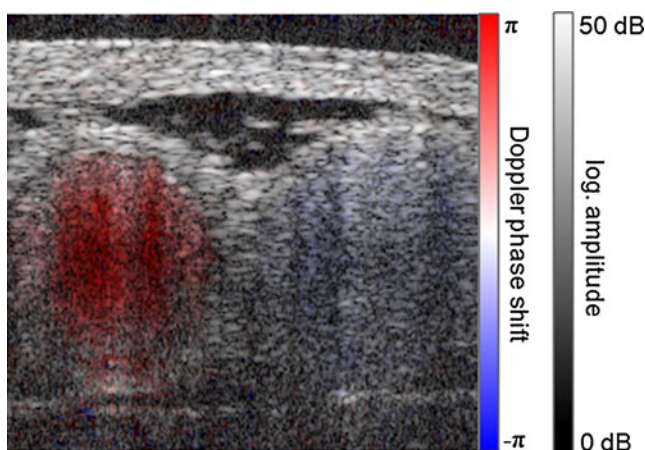


**Fig. 10** Cross-sectional Doppler flow image of the murine artery and vena saphena. The diastolic arterial blood flow is displayed in red and the opposite venous blood flow in blue. The color shown in the Doppler image is generated from the product of the colored velocity scale and the gray amplitude scale

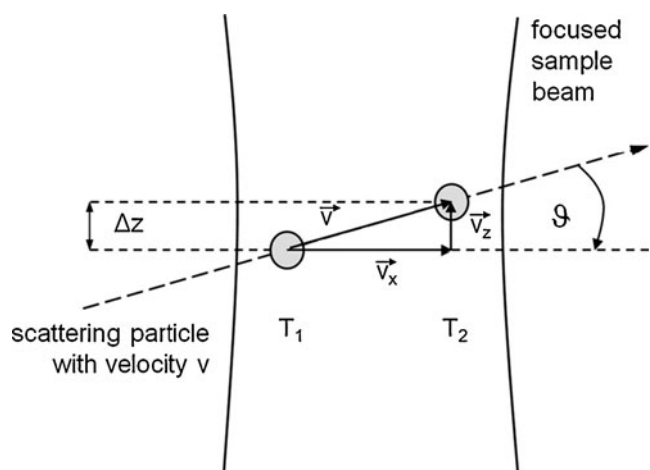


**Fig. 11** Schematic diagram showing the orientation of the velocity vector of sample movement relative to the incident sample beam and the intermediate Doppler angle  $\vartheta$ . ( $\vec{v}$  – absolute sample velocity,  $\vec{v}_z$  – axial,  $\vec{v}_x$  – transverse velocity component)

calculated. But this general assumption is only true for almost purely axial motion. Lately, a new phase-dependent Doppler model for SD OCT was presented which takes the transverse component of the oblique motion into account [151, 152]. This new Doppler model reveals that the effective axial displacement during the integration time is reduced and with this the phase shift is smaller than expected on the basis of the classic Doppler model. It was also shown that for high axial velocity components and, with it, large Doppler angles between the flow and the transverse direction, the classic Doppler model operates as a good approximation with relative deviations smaller than 1%. In contrast with this, for small Doppler angles and high flow velocities the phase shift between adjacent A-scans will approach a constant value making it impossible to quantify the flow velocity. For many in vivo blood-flow measurements, especially 3D flow imaging, random and unpredictable Doppler angles occur so that the undesirable small Doppler angles cannot be precluded. For this case, it has been proposed to extend the limited velocity detection range of the Doppler method in SD OCT by taking the characteristic, flow-dependent signal damping into account [42, 43]. The quantitative combination of Doppler analysis and the signal damping method was presented as a flow phantom study and has shown great promise for extending the limited velocity measurement range of Doppler SD OCT analysis at small Doppler angles and high flow velocities.

#### *Dual-band and spectroscopic OCT*

In OCT, important imaging performance, for example axial resolution and penetration depth into tissue, depend on the spectral properties of the applied light source [153]. Conventional OCT systems are commonly equipped with compact superluminescent diodes (SLDs) emitting in the spectral regions centered around 800 nm or 1300 nm. In general, imaging at shorter wavelengths, i.e. in the region of 800 nm, results in higher axial resolution whereas wavelengths in the region of 1300 nm result in enhanced penetration depth, because of less tissue scattering and

absorption by endogenous chromophores, for example hemoglobin and melanin. The combination of two separate wavelength bands for OCT imaging is referred to as dual-band OCT. These systems were illuminated by two SLDs [154–158] or—for high-resolution OCT—by halogen lamps [159] or broadband supercontinuum lasers [14, 15, 160]. Simultaneous image acquisition in the two common OCT wavelength bands enables combination of enhanced resolution at 800 nm, increased imaging depth at 1300 nm, speckle reduction by means of frequency compounding [156], and extraction of spatially resolved spectral features of the sample from the differential image data obtained. Dual-band imaging has been used for water concentration measurements by differential absorption OCT in phantoms [157] and in the human cornea [158] and for contrast enhancement of soft tissue in the human oral cavity [155], the rabbit trachea [159] and eye [14], and the human nail fold and skin [14, 15, 154, 160]. Figure 12 shows representative dual-band cross-sectional OCT scans of human skin. Higher resolution at 800 nm and an greater imaging depth at 1250 nm are clearly apparent. The spectroscopic sample information obtained with this technique is visualized by use of a color-encoded differential image in which blue and orange represent enhanced backscattering at 800 nm and 1250 nm, respectively. It can be seen that deeper regions are rendered mostly in orange color tones, because of the greater penetration depth at 1250 nm, whereas the superficial regions appear mainly in blue, probably as a result of the enhanced tissue scattering at 800 nm.

Careful interpretation of the spectroscopic content of dual-band data is necessary, especially for birefringent samples. In this situation, birefringence can lead to wavelength-dependent alternations in the OCT signal, because of the polarization-sensitive character of light interferometry. As a consequence, intensity variations between two wavelength bands are not necessarily caused by wavelength-specific absorption and scattering, i.e. spectroscopic sample features, in this case [15]. Figure 13 shows B-scans of the birefringent human fingernail that

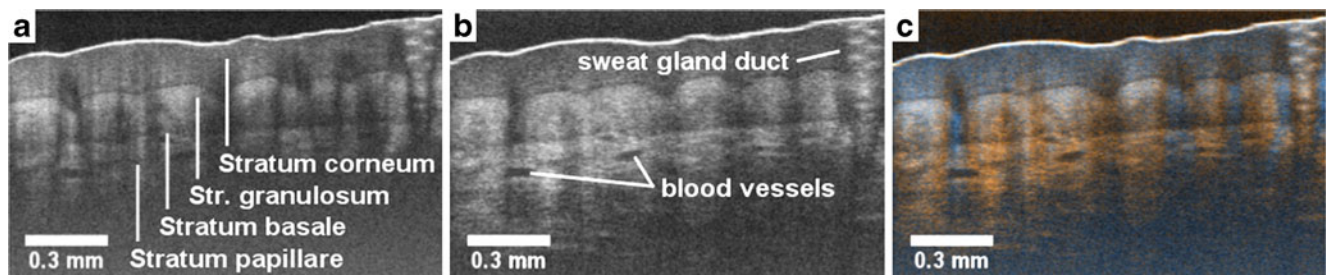


**Fig. 12** Simultaneous dual-band OCT imaging of human skin. Higher resolution at 800 nm (a) and enhanced penetration depth into tissue at 1250 nm (b) is noticeable. Color-encoded differential image (c) with

blue and orange representing enhanced backscattering at 800 nm and 1250 nm, respectively

were simultaneously acquired in the 800 nm and 1300 nm wavelength ranges. The varying depth-dependent intensity alternations in the two spectral bands caused by wavelength-dependent sample birefringence are clearly visible; this leads to apparently wavelength-specific backscattering visualized in the color-encoded differential image.

To further increase the spectral resolution of OCT beyond the two disjunct wavelength bands, the spectral characteristics within one wavelength band must be taken into account. As a result, extraction of spatially resolved spectroscopic sample features by means of time–frequency analysis of the interference pattern in a single wavelength band is referred to as spectroscopic OCT (SOCT). As shown in Fig. 14, the spectra of the backscattered light from the sample are encoded in the envelope of the acquired interference fringe pattern which can be assessed by adequate signal demodulation. It must, however, be remembered there is an inherent tradeoff between spatial and spectral resolution in SOCT. Because of the uncertainty principle, enhancement in spectral resolution results in reduced spatial resolution, and vice versa.

It has been shown that SOCT provides contrast enhancement in comparison with conventional, solely intensity-based OCT [128, 161, 162], although the underlying mechanisms are still not well understood [163]. It has been reported that melanocytes produce a significant red shift to the backscattered light spectrum in the 800 nm wavelength region, probably because of reduced absorption of melanin at longer wavelengths [128, 162]. Besides wavelength-specific absorption of the sample, tissue scattering is important in SOCT. It has been shown that the spectroscopic content of the OCT signal is substantially affected by the size of the scatterers, the size of the sample beam waist, and the mode-inherent speckle noise [163, 164].

One big objective of SOCT is spatially resolved measurement of hemoglobin oxygen saturation level [165, 166]; this was, in part, successfully demonstrated in vitro

for human whole blood [167] and for single red blood cells [168], and in vivo in the human retina [169, 170]. Figure 15 shows OCT imaging of oxygenated and deoxygenated blood samples in the 800 nm wavelength region performed by Liu et al. [171]. Besides cross-sectional imaging, significant oxygen level-related spectra could also be obtained from the OCT signal plotted in Fig. 16.

Detection of specific substances, for example oxy- or deoxyhemoglobin in biological samples, is often referred to as molecular contrast OCT [172]. One prevailing contrast mechanism used is the red or blue shift of the sample spectrum caused by wavelength-dependent extinction of the respective substance. This shift is visualized by color-encoded representation of the spectrum's centroid or center of gravity [128, 162]. A spectral centroid shift can also be provoked by using contrast agents, for example the FDA-approved near-infrared fluorescent dye indocyanine green (ICG) [173]. A major disadvantage of the spectral centroid shift method is its sensitivity to wavelength-dependent scattering. Because scattering in biological tissue is reduced towards longer wavelengths, a non-specific spectral red shift will occur in each turbid medium, especially at greater imaging depths. To overcome this drawback, an alternative method, called spectral triangulation, was reported, again using ICG as contrast agent [174]. In this situation, the OCT signal is obtained at three evenly spaced wavelength intervals. One interval is matched to the dye's absorption maximum and the two others are located below and above this absorption maximum. By means of appropriate processing, the depth-resolved differential dye absorption as the additional contrast can be obtained, while spectral variations of the sample, for example wavelength-dependent scattering, are suppressed to a first approximation. However, use of ICG as an absorptive contrast agent in SOCT is still far from clinical application, because of the high dye concentrations necessary. In general, absorption-based SOCT suffers from a concentration–pathlength compromise. To achieve a sufficient spectral shift of the backscattered light, either a high absorber concentration

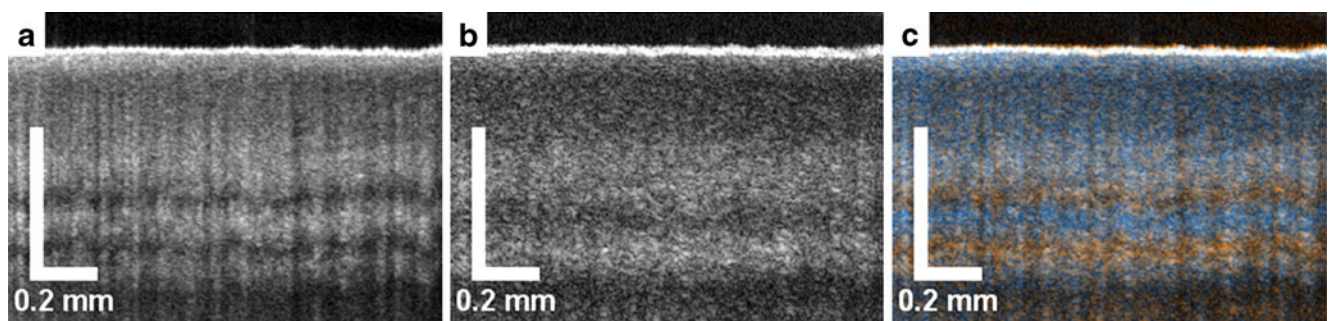


**Fig. 13** Cross-sectional OCT scans of the birefringent human fingernail, simultaneously acquired at 800 nm (a) and 1250 nm (b), and the color-encoded differential image (c). The wavelength-

dependent intensity alternation because of sample birefringence is clearly observable, and leads to apparently wavelength-specific backscattering visualized in (c)



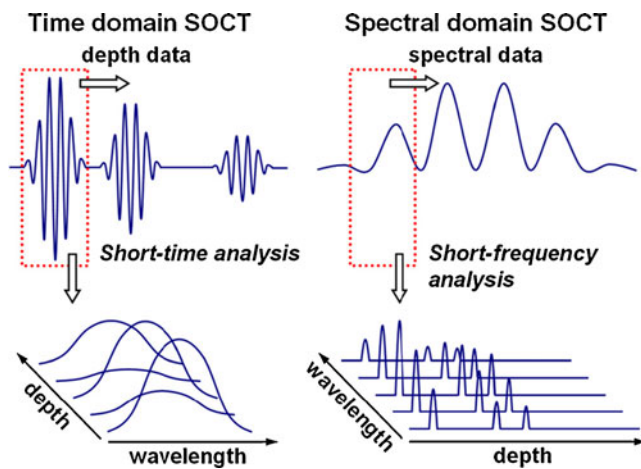


**Fig. 14** Principle of spectroscopic OCT (SOCT) in the time and spectral domain. The depth-resolved spectra of the light backscattered from the sample can be assessed by appropriate demodulation of the acquired interference signals, e.g. by short-time or short-frequency Fourier analysis

must be present or the length of the absorbing region must be large. Therefore, recent developments focus on the more complex scattering-based SOCT [175, 176] which does not suffer from the compromise mentioned above, because wavelength-dependent scattering is almost a point effect [164] depending on the optical properties of individual scatterers and interaction of the scatterers.

#### Polarization-sensitive OCT

Because conventional OCT provides cross-sectional intensity images of backscattered light, polarization-sensitive OCT (PS OCT) is a functional extension using information on the state of polarization of the light to enable 2D and 3D imaging of those properties of optical tissue which change the polarization of light, e.g. birefringence in oriented structures. The major benefits of PS OCT are the contrast enhancement, and the functional differentiation of biological tissue because of their individual optical properties; these make it a very suitable tool for biomedical imaging and segmentation of tissue.

The first PS OCT setups, using low-coherence detection, enabled detection of birefringence [177, 178] and optical axis orientation [179] by simultaneous acquisition of the

interference signals for horizontally and vertically polarized light then calculation of the amplitude ratio and the phase difference, respectively. It is, furthermore, possible to calculate the Jones vector [179] for extraction of the intensity, birefringence, and optical axis orientation. For description of partially polarized light and depolarization properties, the Stokes vector and Mueller matrix formalism [180] are very suitable. Fourier domain detection has also been implemented in PS OCT to obtain both SNR and speed advantage. The amplitude and phase information is thereby immediately accessible after Fourier transformation of the interference spectra. Several spectral domain [181, 182] and OFDI-based PS OCT systems [183, 184] have been reported, with higher A-scan rates up to 62 kHz [184] making PS OCT suitable for in vivo imaging. The development of fiber-based PS OCT systems [182, 183, 185, 186] focusses on use of polarization-maintaining fibers to ensure detection of almost unchanged polarization states during twisting of the fibers. Thus, fiber-based PS OCT systems enable easy alignment of the scanner head, in contrast with bulk optical PS OCT systems, and especially elegant realization of endoscopic applications.

PS OCT has been introduced as an appropriate technique for multiple applications in biological and medical research. First studies have been presented in dermatology, in which PS OCT was used for in vivo birefringence imaging of photoaged skin [187, 188] demonstrating the relationship between dermal birefringence and skin roughness. A further study has differentiated basal cell carcinoma from normal tissue in intensity images and, especially, in birefringence images [189] pointing out the potential for intra-operative guidance. Differentiation of tissue by PS OCT has also been used for assessment of collagen disorganization in ruptured Achilles tendons [190]. As a further pre-clinical research study, the smooth muscle cell and the collagen content in arteriosclerotic plaques have been investigated by PS OCT ex vivo imaging [191] and could be related to the birefringence. This additional information generated by PS OCT is likely to be used for intracoronary evaluation and identification of plaque instabilities. Endoscopic PS OCT has been used for in vivo vocal fold imaging [192], using a MEMS scanning catheter. In this work, PS OCT as a noninvasive endoscopic imaging technique, in combination with wide-field imaging, was demonstrated to be an

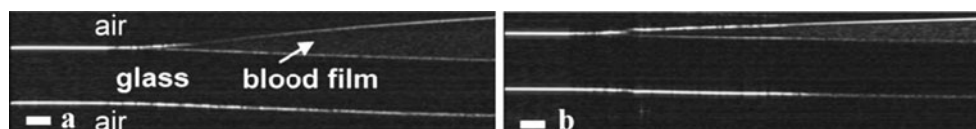
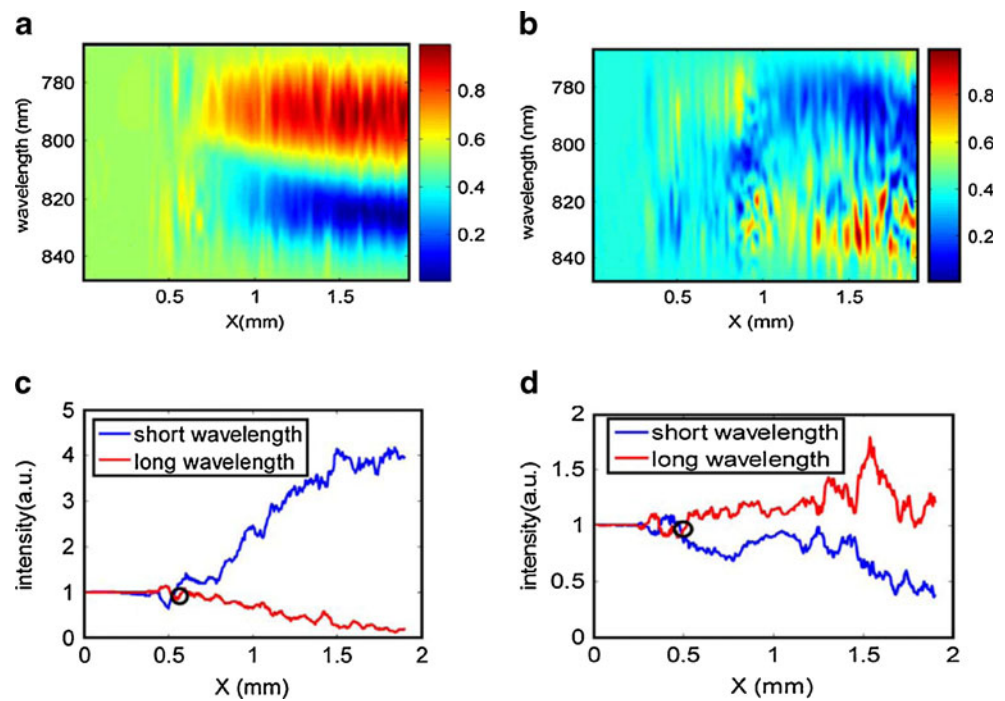


**Fig. 15** OCT cross-sectional images of oxygenated (a) and deoxygenated (b) blood samples on a glass slide, acquired in the 800 nm wavelength region. The bar represents 100  $\mu\text{m}$ . (Courtesy of Xuan

Liu from Johns Hopkins University in Baltimore, image reprinted from Ref. [171]; © 2010 IEEE



**Fig. 16** Local spectra of a glass slide surface partially coated with oxygenated (a) and deoxygenated (b) blood as shown in Fig. 15. Greater absorption toward longer wavelengths by oxygenated blood and toward shorter wavelengths by deoxygenated blood is clearly identifiable. Local spectral intensity of the glass slide surface in the short-wavelength (771–792 nm) and long-wavelength (819–848 nm) regions vs. lateral position obtained from oxygenated (c) and deoxygenated (d) blood. (Courtesy of Xuan Liu from Johns Hopkins University in Baltimore, image reprinted from Ref. [171]; © 2010 IEEE



appropriate method for visualization of the spatial extension of vocal fold lesions. In ophthalmology, PS OCT systems have been established for analysis of human cornea [193] and the retinal layered structures [194, 195]. The latest publications [182, 196] focus, especially, on the segmentation of the retinal pigment epithelium (RPE), which can also be classified, on the basis of its depolarization property, in patients suffering from age-related macular degeneration in which the distorted RPE layer is hardly identifiable with standard OCT imaging. In addition to retardation and optic axis orientation, the degree of polarization uniformity (DOPU), representing the polarization scrambling tissue property, has been calculated for segmentation of the RPE layer. For instance, the reflectivity B-scan and the DOPU image of a healthy human retina are compared in Fig. 17 [196]. Beside these ophthalmic applications, PS OCT has recently been reported for in vivo visualization of cancer tissue in mouse and hamster models [197]. In the murine cancer model, subcutaneously injected cancer cells of a human pancreatic cancer cell line have been observed, in a longitudinal study, over ten days after injection. Because of the different tissue birefringence, PS OCT enables a clear differentiation of cancer tissue while retaining the advantage of noninvasive imaging.

#### *Combination with complementary optical methods*

As the preceding examples have shown, OCT enables 3D, noninvasive, contactless, microscale imaging, because of the scattering of infrared light by cellular and subcellular

structures, for widespread applications. Nevertheless, information is still lacking on the molecular constituents embedded in the sample. As an advanced approach, it has been shown that combination of OCT with complementary optical methods, for example fluorescence imaging techniques [198–200] or, very recently, coherent anti-Stokes Raman spectroscopy (CARS) [201] has the ability to reveal the chemical composition of tissue structures, thereby expanding the yield of information. Furthermore, the horizontal 2D map given by optical en-face sectioning techniques, for example confocal fluorescence microscopy, helps orienting and positioning of the OCT scanning field and enables targeted tissue studies, as shown, for instance, for drosophila heart monitoring [202].

For integration of additional optical methods in a conventional OCT system, dichroic mirrors are introduced into the optical path for spectral combination of the near-infrared OCT beam with the technique's excitation light. In fluorescence techniques, linear single photon excitation and nonlinear multiphoton applications, using a femtosecond laser source, are possible. For CARS, two pulsed lasers spectrally shifted by a substance-specific transition energy have to be applied. Depending on the usage of external fluorophores, for example ALA or ICG, or endogenous fluorescence, e.g. NADH, elastin, collagen, or lipids, the excitation light sources have to be chosen on the basis of the excitation and transition spectra of the target molecule.

An example of such combined molecular and geometrical data is shown in Fig. 18 for fixed rabbit lung tissue. A dissected sample was stained with sulforhodamine B

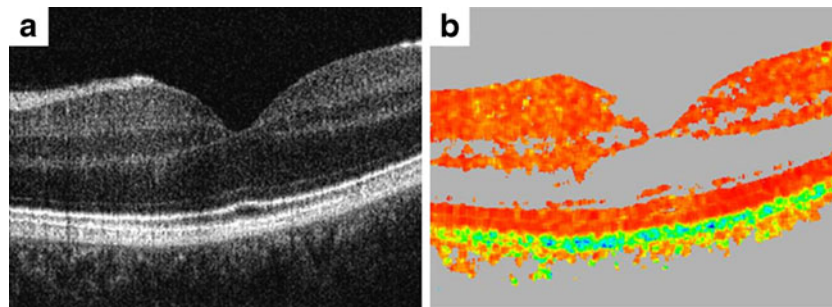


**Fig. 17** Structural (a) and DOPU B-scan (b) as examples of polarization-sensitive OCT of the fovea region of the healthy human retina. DOPU values range from 0 (dark blue) to 1 (red). (Courtesy of

Christoph Hitzenberger from Medical University of Vienna, image reprinted from Ref. [196] with permission of SPIE)

(SRB), a dye specifically binding to the biomolecule elastin. Three-dimensional OCT is displayed as a gray scale image whereas SRB fluorescence, indicating the fibrous distribution of the extracellular matrix molecule elastin, is shown in red.

One of the main applications of combined methods is in ophthalmological studies. In such studies, simultaneous use of ICG-mediated angiography, scanning laser ophthalmology (SLO), and retina OCT imaging [203] with additional combinations of fluorescein angiography and fundus autofluorescence (FAF) detection [204, 205] has been achieved. These features are already in use in the commercially available instrument Spectralis HRA + OCT (Heidelberg Engineering, Germany) and provide a means of diagnosing such diseases as macular degeneration and loss of retinal transparency because of acute retinal artery occlusion [204].

In cancer studies, the power of joint complementary techniques is used on the one hand for the detection of suspicious areas revealed by fluorescence markers, e.g. ALA and HAL, by staining of cells with an increased

metabolic activity, and, on the other hand, for differentiation between malignant and benign tissue using OCT [206–208]. A more advanced approach involves fluorescence lifetime maps of oral epithelial cancer showing distributions of the metabolic coenzymes NADH and FAD within the thicker tumor area, previously revealed by OCT volume scans, and collagen fluorescence in the thinner adjacent region [209].

Functional imaging, for example cell adhesion to microtextured substrates or cell–substrate interactions, is facilitated by multiphoton excitation of green fluorescent protein (GFP) attached to the focal adhesion molecule vinculin, as shown in several studies [210–212]. In these reports, optical coherence microscopy (OCM) has been used to detect substrate topology whereas multiphoton microscopy (MPM) shows the presence of vinculin and the cellular nuclei. In fact, the high lateral resolution of OCM and the additional phase information of the interference signal makes it possible to obtain phase images of cells and even resolve their actin skeleton. These findings were confirmed by applying two-photon excited fluorescence of Alexa Fluor 488 phalloidin-labeled actin filaments in fixed *mntjak* skin fibroblast cells [213].

The variety of applications mentioned above for OCT combined with complementary optical methods are indicative of increasing interest in the study of structural and functional details and dependencies in biomedical samples. With these techniques, obtaining increasing amounts of information becomes feasible with one experiment only, enabling thorough understanding of biophysical, biochemical, and biomedical processes.

## Conclusion

As shown above, optical coherence tomography (OCT) is a rapidly developing, powerful imaging technique for use in biomedical research and in pre-clinical and clinical medi-

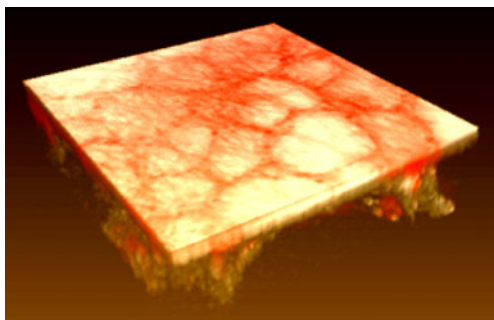


**Fig. 18** 3D image of a fixed rabbit lung stained with the elastin-binding dye sulforhodamine B (SRB). The geometrical structure arising from the OCT data is displayed in *gray scale*, the network of elastin fibers is revealed by SRB fluorescence indicated in *red*. Alveolar structures are clearly visible both in the OCT and the fluorescence image. In addition, OCT shows a bright backscattering plane which is assigned to the *pleura visceralis*. Sample size ( $x \times y \times z$ ):  $320 \mu\text{m} \times 320 \mu\text{m} \times 113 \mu\text{m}$

cine. In this review, the ability to conduct non-excisional “optical biopsy”, with a focus on visualization of morphological and physiological properties, and the resulting potential, especially for fundamental research, has been reported. In recent years, a huge increase of applications, which exceed the simple term “optical biopsy”, enabling in vivo and in situ imaging for examination of tissue microstructures and pathology, can be recognized. The end has not yet been reached. The large number of OCT applications has resulted from increased imaging speed and the consequentially reduced motion artifacts, which has substantially improved dynamic in vivo imaging. This speed increase benefits fundamental biomedical research in, e.g., Doppler OCT and embryonic OCT imaging not only in developmental biology but, of course, also in clinical studies, for example ophthalmological and intravascular OCT imaging [214]. Current high-speed OCT systems are generally based on FD OCT technology, as a result of which imaging speed is almost unrestricted owing to novel developments in optical technology, for example faster detectors and new broadband light sources. Consequently, FD OCT systems are most frequently used, because of the feasibility of real-time 3D imaging. Advances in OCT are not only based on technology improving imaging speed, however, but also on new technical developments and advanced imaging techniques. Examples are polarization-sensitive OCT for the imaging of the birefringence properties of biological tissue, indicative of fiber organization, second harmonic OCT for contrast and resolution enhancement of conventional OCT to image changes in molecular structure of tissue [215], contrast agent OCT using microspheres with, e.g., embedded gold nanoparticles for enhanced contrast in spectroscopic and conventional intensity-based OCT images [216], and magnetomotive OCT using magnetic agents and a modulated external magnetic field to achieve molecular contrast in OCT [217]. Other publications focus on such areas as numerical dispersion compensation, novel scanning techniques, and sample-specific probe designs. As a result of the variety of developments due to emerging biomedical and clinical challenging questions, the basis is provided for custom-designed multimodal OCT systems for determination of high-quality biological data both for fundamental research and for medical diagnosis and therapy. The most prevalent clinical application of OCT is imaging of the eye fundus, advances in intravascular surgical diagnostics, guidance, and intervention with routine use of OCT are conceivable. As was shown in this review, OCT also has great potential for a wide field of applications in biomedicine, for example small-animal fundamental research, developmental biology, and tissue engineering. Because OCT is largely unspecific for homogenous biological samples, for example cerebral tissue, with structures smaller than half the central

wavelength, studies searching for tissue classification are of interest to scientists also. With identification of an applicable classification, OCT could then also achieve a breakthrough in the early detection of cancer by the differentiation of non and neoplastic tissue. The auspicious technique optical coherence microscopy (OCM), providing en-face images with high transverse spatial resolution, because of higher numerical aperture focusing than traditional OCT, could be very helpful in early cancer diagnosis by enabling cellular level imaging. Finally, fields of application in fundamental biomedical research and clinical medicine, and industrial utilization, are not yet completely exploited; this in turn will initiate future hardware and software developments in OCT.

**Acknowledgements** This research was supported by the following institutions and funds: SAB (Sächsische Aufbaubank, project 11261/1759), funding from the European Union (ESF) and the Free State of Saxony (project 080937940), the BMBF (Bundesministerium für Bildung und Forschung, NBL 3 and project 03NUK010I), the MeDDrive program of the Faculty of Medicine Carl Gustav Carus of Dresden University of Technology and the German Research Foundation (DFG) “Protective Artificial Respiration” (PAR) - KO 1814/6-1, KO 1814/6-2 and KU 1218/4-1.

Furthermore, the authors would like to thank Dr Gregor Müller from the Vascular Endothelium and Microcirculation group of Professor Morawietz (Faculty of Medicine Carl Gustav Carus, Dresden University of Technology, Germany), the group of Dr Marius Ader (Aline Höfer, Dierk Wittig; Center for Regenerative Therapies, Dresden, and Institute of Anatomy, Faculty of Medicine Carl Gustav Carus, Dresden University of Technology, Germany), and, finally, the group of Professor W.M. Kübler (Institute of Physiology, Charité Berlin, Germany and St. Michael’s Hospital, Toronto, Canada) for all their support and for providing biological samples.

## References

1. Michelson AA (1881) *Am J Sci* 22:120–129
2. Huang D, Swanson EA, Lin CP, Schuman JS, Stinson WG, Chang W, Hee MR, Flotte T, Gregory K, Puliafito CA, Fujimoto JG (1991) *Science* 254:1178–1181
3. Steiner G (2010) *Anal Bioanal Chem* 397:903–904
4. Fercher AF, Mengedocht K, Werner W (1988) *Opt Lett* 13:186–188
5. Hitzenberger CK (1991) *Invest Ophthalmol Vis Sci* 32:616–624
6. Tearney GJ, Brezinski ME, Bouma BE, Boppart SA, Pitris C, Southern JF, Fujimoto JG (1997) *Science* 276:2037–2039
7. Vakoc BJ, Shishko M, Yun SH, Oh WY, Suter MJ, Desjardins AE, Evans JA, Nishioka NS, Tearney GJ, Bouma BE (2007) *Gastrointest Endosc* 65:898–905
8. Tearney GJ, Jang IK, Bouma BE (2006) *J Biomed Opt* 11:021002
9. Povazay B, Hermann B, Unterhuber A, Hofer B, Sattmann H, Zeiler F, Morgan JE, Falkner-Radler C, Glittenberg C, Blinder S, Drexler W (2007) *J Biomed Opt* 12:041211
10. Unterhuber A, Povazay B, Hermann B, Sattmann H, Chavez-Pirson A, Drexler W (2005) *Opt Express* 13:3252–3258
11. Drexler W, Morgner U, Kärtner FX, Pitris C, Boppart SA, Li XD, Ippen EP, Fujimoto JG (1999) *Opt Lett* 24:1221–1223
12. Ko T, Adler D, Fujimoto J, Mamedov D, Prokhorov V, Shidlovski V, Yakubovich S (2004) *Opt Express* 12:2112–2119

13. Szkulmowski M, Wojtkowski M, Bajraszewski T, Gorczynska I, Targowski P, Wasilewski W, Kowalczyk A, Radzewicz C (2005) *Opt Commun* 246:569–578
14. Spöler F, Kray S, Grychtol P, Hermes B, Bornemann J, Först M, Kurz H (2007) *Opt Express* 15:10832–10841
15. Cimalla P, Walther J, Mehner M, Cuevas M, Koch E (2009) *Opt Express* 17:19486–19500
16. Qi B, Himmer AP, Gordon LM, Yang XDV, Dickensheets LD, Vitkin IA (2004) *Opt Commun* 232:123–128
17. Schmitt JM, Lee SL, Yung KM (1997) *Opt Commun* 142:203–207
18. Kim YK, Kim YP (2010) *Opt Eng* 49:055601
19. Gao W (2007) *Appl Opt* 46:986–992
20. Rollins AM, Kulkarni MD, Yazdanfar S, Ung-arunyawee R, Izatt JA (1998) *Opt Express* 3:219–229
21. Fercher AF, Hitzinger CK, Kamp G, El-Zaiat SY (1995) *Opt Commun* 117:43–48
22. Bail MA, Haeusler G, Herrmann JM, Lindner MW, Ringler R (1996) In: Benaron DA, Chance B, Mueller GJ (eds) *SPIE, Vienna, Austria*, 298–303
23. Hausler G, Lindner MW (1998) *J Biomed Opt* 3:21–31
24. Leitgeb R, Hitzinger C, Fercher A (2003) *Opt Express* 11:889–894
25. Choma M, Sarunic M, Yang C, Izatt J (2003) *Opt Express* 11:2183–2189
26. de Boer JF, Cense B, Park BH, Pierce MC, Tearney GJ, Bouma BE (2003) *Opt Lett* 28:2067–2069
27. Wieser W, Biedermann BR, Klein T, Eigenwillig CM, Huber R (2010) *Opt Express* 18:14685–14704
28. Wojtkowski M, Srinivasan V, Ko T, Fujimoto J, Kowalczyk A, Duker J (2004) *Opt Express* 12:2404–2422
29. Wang RK, Jacques SL, Ma Z, Hurst S, Hanson SR, Gruber A (2007) *Opt Express* 15:4083–4097
30. Vakhtin AB, Kane DJ, Wood WR, Peterson KA (2003) *Appl Opt* 42:6953–6958
31. Kang JU, Han JH, Liu X, Zhang K (2010) *J Opt Soc Korea* 14:1–13
32. Koch E, Hammer D, Wang S, Cuevas M, Walther J (2009) In: Andersen PE, Bouma BE (eds) *SPIE, Munich, Germany*, 737220
33. Akcay AC, Rolland JP, Eichenholz JM (2003) *Opt Lett* 28:1921–1923
34. Bower BA, Zhao M, Zawadzki RJ, Izatt JA (2007) *J Biomed Opt* 12:041214
35. Vergnole S, Levesque D, Lamouche G (2010) *Opt Express* 18:10446–10461
36. Traub WA (1990) *J Opt Soc Am A* 7:1779–1791
37. Hu Z, Rollins AM (2007) *Opt Lett* 32:3525–3527
38. Eigenwillig CM, Biedermann BR, Wieser W, Huber R (2009) *Opt Express* 17:18794–18807
39. Hauger C, Wörz M, Hellmuth T (2003) *Appl Opt* 42:3896–3902
40. Bajraszewski T, Wojtkowski M, Szkulmowski M, Szkulmowska A, Huber R, Kowalczyk A (2008) *Opt Express* 16:4163–4176
41. Liu B, Brezinski ME (2007) *J Biomed Opt* 12:044007
42. Walther J, Krüger A, Cuevas M, Koch E (2008) *J Opt Soc Am A* 25:2791–2802
43. Walther J, Mueller G, Morawietz H, Koch E (2010) *J Biomed Opt* 15:041511
44. Changho C, Morosawa A, Sakai T (2008) *IEEE J Quantum Electron* 14:235–242
45. Hughes M, Spring M, Podoleanu A (2010) *Appl Opt* 49:99–107
46. Huber R, Wojtkowski M, Fujimoto JG (2006) *Opt Express* 14:3225–3237
47. Biedermann BR, Wieser W, Eigenwillig CM, Klein T, Huber R (2009) *Opt Express* 17:9947–9961
48. Drexler W, Fujimoto JG (2008) *Prog Retin Eye Res* 27:45–88
49. Wolf-Schnurbusch UEK, Ceklic L, Brinkmann CK, Iliev ME, Frey M, Rothenbuehler SP, Enzmann V, Wolf S (2009) *Invest Ophthalmol Vis Sci* 50:3432–3437
50. Povazay B, Bizheva K, Hermann B, Unterhuber A, Sattmann H, Fercher A, Drexler W, Schubert C, Ahnelt P, Mei M, Holzwarth R, Wadsworth W, Knight J, Russell PS (2003) *Opt Express* 11:1980–1986
51. Povazay B, Hofer B, Torti C, Hermann B, Tumlinson AR, Esmaelpour M, Egan CA, Bird AC, Drexler W (2009) *Opt Express* 17:4134–4150
52. Zhang Y, Cense B, Rha J, Jonnal RS, Gao W, Zawadzki RJ, Werner JS, Jones S, Olivier S, Miller DT (2006) *Opt Express* 14:4380–4394
53. Fernández EJ, Hermann B, Povazay B, Unterhuber A, Sattmann H, Hofer B, Ahnelt PK, Drexler W (2008) *Opt Express* 16:11083–11094
54. Horio N, Kachi S, Hori K, Okamoto Y, Yamamoto E, Terasaki H, Miyake Y (2001) *Arch Ophthalmol* 119:1329–1332
55. Nagata A, Higashide T, Ohkubo S, Takeda H, Sugiyama K (2009) *Invest Ophthalmol Vis Sci* 50:2809–2815
56. Kocaoglu OP, Uhlhorn SR, Hernandez E, Juarez RA, Will R, Parel JM, Manns F (2007) *Invest Ophthalmol Vis Sci* 48:1283–1289
57. Ruggeri M, Wehbe H, Jiao S, Gregori G, Jockovich ME, Hackam A, Duan Y, Puliafito CA (2007) *Invest Ophthalmol Vis Sci* 48:1808–1814
58. Huber G, Beck SC, Grimm C, Sahaboglu-Tekgoz A, Paquet-Durand F, Wenzel A, Humphries P, Redmond TM, Seeliger MW, Fischer MD (2009) *Invest Ophthalmol Vis Sci* 50:5888–5895
59. Harii S, Moayed AA, Dracopoulos A, Hyun C, Boyd S, Bizheva K (2009) *Opt Express* 17:24304–24316
60. Li Q, Timmers AM, Hunter K, Gonzalez-Pola C, Lewin AS, Reitze DH, Hauswirth WW (2001) *Invest Ophthalmol Vis Sci* 42:2981–2989
61. Srinivasan VJ, Ko TH, Wojtkowski M, Carvalho M, Clermont A, Bursell SE, Song QH, Lem J, Duker JS, Schuman JS, Fujimoto JG (2006) *Invest Ophthalmol Vis Sci* 47:5522–5528
62. Kim KH, Puoris'haag M, Maguluri GN, Umino Y, Cusato K, Barlow RB, de Boer JF (2008) *J Vis* 8:1701–1711
63. Wang L, Hofer B, Chen YP, Guggenheim JA, Drexler W, Povazay B (2010) *J Biomed Opt* 15:046004
64. Zhou X, Xie J, Shen M, Wang J, Jiang L, Qu J, Lu F (2008) *Vis Res* 48:1137–1143
65. Moayed AA, Hariri S, Hyun C, Doran B, Kraft TW, Boyd S, Bizheva K (2010) *J Biomed Opt* 15:040506
66. Mertens M, Tabuchi A, Meissner S, Krueger A, Schirrmann K, Kertzscher U, Pries AR, Slutsky AS, Koch E, Kuebler WM (2009) *Crit Care Med* 37:2604–2611
67. Yin Y, Hoffman EA, Lin CL (2009) *Med Phys* 36:4213–4222
68. Mathew L, Gaede S, Wheatley A, Etemad-Rezai R, Rodrigues GB, Parraga G (2010) *Med Phys* 37:22–31
69. Sznitman J, Sutter R, Altorf D, Stapanoni M, Rösger T, Schittny J (2010) *J Visualization* 13:337–345
70. Meissner S, Knels L, Koch E (2009) *J Biomed Opt* 14:064037
71. Meissner S, Knels L, Schnabel C, Koch T, Koch E (2010) *J Biomed Opt* 15:016030
72. Popp A, Wendel M, Knels L, Koch T, Koch E (2006) *J Biomed Opt* 11:014015
73. Meissner S, Knels L, Krueger A, Koch T, Koch E (2009) *J Biomed Opt* 14:054020
74. Tabuchi A, Mertens M, Kuppe H, Pries AR, Kuebler WM (2008) *J Appl Physiol* 104:338–346
75. Meissner S, Tabuchi A, Mertens M, Kuebler WM, Koch E (2010) *J Biomed Opt* 15:036016
76. Silva MR, Shen HT, Marzban A, Gouldstone A (2010) *J Healthc Eng* 1:415–433
77. Coxson HO, Quiney B, Sin DD, Xing L, McWilliams AM, Mayo JR, Lam S (2008) *Am J Respir Crit Care Med* 177:1201–1206



78. Lam S, Standish B, Baldwin C, McWilliams A, leRiche J, Gazdar A, Vitkin AI, Yang V, Ikeda N, MacAulay C (2008) *Clin Cancer Res* 14:2006–2011
79. Xie T, Liu G, Kreuter K, Mahon S, Colt H, Mukai D, Peavy GM, Chen Z, Brenner M (2009) *J Biomed Opt* 14:064045
80. Tearney GJ, Boppart SA, Bouma BE, Brezinski ME, Weissman NJ, Southern JF, Fujimoto JG (1996) *Opt Lett* 21:543–545
81. Boppart SA, Bouma BE, Pitris C, Tearney GJ, Fujimoto JG, Brezinski ME (1997) *Opt Lett* 22:1618–1620
82. Yaqoob Z, Wu J, McDowell EJ, Heng X, Yang C (2006) *J Biomed Opt* 11:063001
83. Bezerra HG, Costa MA, Guagliumi G, Rollins AM, Simon DI (2009) *J Am Coll Cardiol Interv* 2:1035–1046
84. Suter MJ, Vakoc BJ, Yachimski PS, Shishkov M, Lauwers GY, Mino-Kenudson M, Bouma BE, Nishioka NS, Tearney GJ (2008) *Gastrointest Endosc* 68:745–753
85. Li X, Chudoba C, Ko T, Pitris C, Fujimoto JG (2000) *Opt Lett* 25:1520–1522
86. Tumlinson AR, Povazay B, Hariri LP, McNally J, Unterhuber A, Hermann B, Sattmann H, Drexler W, Barton JK (2006) *J Biomed Opt* 11:064003–064008
87. Herz PR, Chen Y, Aguirre AD, Schneider K, Hsiung P, Fujimoto JG, Madden K, Schmitt J, Goodnow J, Petersen C (2004) *Opt Lett* 29:2261–2263
88. Xi J, Huo L, Wu Y, Cobb MJ, Hwang JH, Li X (2009) *Opt Lett* 34:1943–1945
89. Fu HL, Leng Y, Cobb MJ, Hsu K, Hwang JH, Li X (2008) *J Biomed Opt* 13:060502–060503
90. Wu J, Conry M, Gu C, Wang F, Yaqoob Z, Yang C (2006) *Opt Lett* 31:1265–1267
91. Pan Y, Li Z, Xie T, Chu CR (2003) *J Biomed Opt* 8:648–654
92. Xie T, Guo S, Chen Z, Mukai D, Brenner M (2006) *Opt Express* 14:3238–3246
93. Aguirre AD, Hertz PR, Chen Y, Fujimoto JG, Piyawattanametha W, Fan L, Wu MC (2007) *Opt Express* 15:2445–2453
94. Kim KH, Park BH, Maguluri GN, Lee TW, Rogomentich FJ, Bancu MG, Bouma BE, de Boer JF, Bernstein JJ (2007) *Opt Express* 15:18130–18140
95. Bouma BE, Tearney GJ, Compton CC, Nishioka NS (2000) *Gastrointest Endosc* 51:467–474
96. Cobb MJ, Hwang JH, Upton MP, Chen Y, Oelschlagel BK, Wood DE, Kimmey MB, Li X (2010) *Gastrointest Endosc* 71:223–230
97. Chen Y, Aguirre AD, Hsiung PL, Desai S, Herz PR, Pedrosa M, Huang Q, Figueiredo M, Huang SW, Koski A, Schmitt JM, Fujimoto JG, Mashimo H (2007) *Endoscopy* 39:599–605
98. Hatta W, Uno K, Koike T, Yokosawa S, Iijima K, Imatani A, Shimosegawa T (2010) *Gastrointest Endosc* 71:899–906
99. Brezinski ME (2006) *Int J Cardiol* 107:154–165
100. Yang VXD, Gordon M, Tang SJ, Marcon N, Gardiner G, Qi B, Bisland S, Seng-Yue E, Lo S, Pekar J, Wilson B, Vitkin I (2003) *Opt Express* 11:2416–2424
101. Yang VXD, Tang SJ, Gordon ML, Qi B, Gardiner G, Cirocco M, Kortan P, Haber GB, Kandel G, Vitkin IA, Wilson BC, Marcon NE (2005) *Gastrointest Endosc* 61:879–890
102. Guo S, Yu L, Seppehr A, Perez J, Su J, Ridgway JM, Vokes D, Wong BJF, Chen Z (2009) *J Biomed Opt* 14:014017
103. Whiteman SC, Yang Y, van Pittius DG, Stephens M, Parmer J, Spiteri MA (2006) *Clin Cancer Res* 12:813–818
104. Wilder-Smith P, Lee K, Guo S, Zhang J, Osann K, Chen Z, Messadi D (2009) *Lasers Surg Med* 41:353–357
105. Arvanitakis M, Hookey L, Tessier G, Demetter P, Nagy N, Stellke A, De Maertelaer V, Devière J, Le Moine O (2009) *Endoscopy* 41:696–701
106. Singh P, Chak A, Willis JE, Rollins A, Sivak J (2005) *Gastrointest Endosc* 62:970–974
107. Mueller-Lisse UL, Bader M, Bauer M, Engelram E, Hocaoglu Y, Püls M, Meissner OA, Babaryka G, Sroka R, Stief CG, Reiser MF, Mueller-Lisse UG (2010) *Med Laser Appl* 25:44–52
108. Jemal A, Siegel R, Xu J, Ward E (2010) *CA Cancer J Clin* 60:277–300
109. Jesser CA, Boppart SA, Pitris C, Stamper DL, Nielsen GP, Brezinski ME, Fujimoto JG (1999) *Br J Radiol* 72:1170–1176
110. Li XD, Boppart SA, Van Dam J, Mashimo H, Mutinga M, Drexler W, Klein M, Pitris C, Krinsky ML, Brezinski ME, Fujimoto JG (2000) *Endoscopy* 32:921–930
111. Michel RG, Kinasewitz GT, Fung KM, Keddissi JI (2010) *Chest* 138:984–988
112. Vokes DE, Jackson R, Guo SG, Perez JA, Su JP, Ridgway JM, Armstrong WB, Chen ZP, Wong BJF (2008) *Ann Otol Rhinol Laryngol* 117:538–547
113. Pitris C, Goodman A, Boppart SA, Libus JJ, Fujimoto JG, Brezinski ME (1999) *Obstet Gynecol* 93:135–139
114. Luo W, Nguyen FT, Zysk AM, Ralston TLS, Brockenbrough J, Marks DL, Oldenburg AL, Boppart SA (2005) *Technol Cancer Res Treat* 4:539–547
115. Boppart S, Luo W, Marks D, Singletary K (2004) *Breast Cancer Res Treat* 84:85–97
116. Zysk AM, Nguyen FT, Oldenburg AL, Marks DL, Boppart SA (2007) *J Biomed Opt* 12:051403
117. Böhringer H, Lankenau E, Stellmacher F, Reusche E, Hüttmann G, Giese A (2009) *Acta Neurochir* 151:507–517
118. Nguyen FT, Zysk AM, Chaney EJ, Adie SG, Kotynek JG, Oliphant UJ, Bellafiore FJ, Rowland KM, Johnson PA, Boppart SA (2010) *IEEE Eng Med Biol Mag* 29:63–70
119. Nguyen FT, Zysk AM, Chaney EJ, Kotynek JG, Oliphant UJ, Bellafiore FJ, Rowland KM, Johnson PA, Boppart SA (2009) *Cancer Res* 69:8790–8796
120. Fujimoto JG, Pitris C, Boppart SA, Brezinski ME (2000) *Neoplasia* 2:9–25
121. Zysk AM, Boppart SA (2006) *J Biomed Opt* 11:054015–054017
122. Vakoc BJ, Lanning RM, Tyrrell JA, Padera TP, Bartlett LA, Stylianopoulos T, Munn LL, Tearney GJ, Fukumura D, Jain RK, Bouma BE (2009) *Nat Med* 15:1219–1223
123. Sokolov K, Follen M, Aaron J, Pavlova I, Malpica A, Lotan R, Richards-Kortum R (2003) *Cancer Res* 63:1999–2004
124. Halcox JPJ, Schenke WH, Zalos G, Mincemoyer R, Prasad A, Waclawiw MA, Nour KRA, Quyyumi AA (2002) *Circulation* 106:653–658
125. Eichhorn B, Muller G, Leuner A, Sawamura T, Ravens U, Morawietz H (2009) *Cardiovasc Res* 82:493–502
126. Meissner S, Muller G, Walther J, Morawietz H, Koch E (2009) *J Biomed Opt* 14:034027
127. Muller G, Meissner S, Walther J, Cuevas M, Koch E, Morawietz H (2009) *Horm Metab Res* 41:537–541
128. Morgner U, Drexler W, Kärtner FX, Li XD, Pitris C, Ippen EP, Fujimoto JG (2000) *Opt Lett* 25:111–113
129. Leitgeb R, Wojtkowski M, Kowalczyk A, Hitzenberger CK, Sticker M, Fercher AF (2000) *Opt Lett* 25:820–822
130. Wang RK, Ma Z, Kirkpatrick SJ (2006) *Appl Phys Lett* 89:144103
131. Kirkpatrick SJ, Wang RK, Duncan DD (2006) *Opt Express* 14:11585–11597
132. Wang XJ, Milner TE, Nelson JS (1995) *Opt Lett* 20:1337–1339
133. Chen Z, Milner TE, Srinivas S, Wang X, Malekafzali A, van Gemert MJC, Nelson JS (1997) *Opt Lett* 22:1119–1121
134. Chen Z, Milner TE, Dave D, Nelson JS (1997) *Opt Lett* 22:64–66
135. Izatt JA, Kulkarni MD, Yazdanfar S, Barton JK, Welch AJ (1997) *Opt Lett* 22:1439–1441
136. Xu Z, Carrion L, Maciejko R (2008) *Opt Express* 16:4394–4412
137. Ren H, Brecke KM, Ding Z, Zhao Y, Nelson JS, Chen Z (2002) *Opt Lett* 27:409–411

138. White B, Pierce M, Nassif N, Cense B, Park B, Tearney G, Bouma B, Chen T, de Boer J (2003) *Opt Express* 11:3490–3497
139. Leitgeb R, Schmetterer L, Drexler W, Fercher A, Zawadzki R, Bajraszewski T (2003) *Opt Express* 11:3116–3121
140. Schmoll T, Kolbitsch C, Leitgeb RA (2009) *Opt Express* 17:4166–4176
141. Mariampillai A, Standish BA, Munce NR, Randall C, Liu G, Jiang JY, Cable AE, Vitkin IA, Yang VXD (2007) *Opt Express* 15:1627–1638
142. Vakoc B, Yun S, de Boer J, Tearney G, Bouma B (2005) *Opt Express* 13:5483–5493
143. Walther J, Mueller G, Morawietz H, Koch E (2009) *Sens Actuator A Phys* 156:14–21
144. Yun SH, Tearney G, de Boer J, Bouma B (2004) *Opt Express* 12:2977–2998
145. Szkulmowski M, Szkulmowska A, Bajraszewski T, Kowalczyk A, Wojtkowski M (2008) *Opt Express* 16:6008–6025
146. Szkulmowska A, Szkulmowski M, Szlag D, Kowalczyk A, Wojtkowski M (2009) *Opt Express* 17:10584–10598
147. Tao YK, Davis AM, Izatt JA (2008) *Opt Express* 16:12350–12361
148. Tao YK, Kennedy KM, Izatt JA (2009) *Opt Express* 17:4177–4188
149. Bachmann AH, Villiger ML, Blatter C, Lasser T, Leitgeb RA (2007) *Opt Express* 15:408–422
150. Zhang J, Chen Z (2005) *Opt Express* 13:7449–7457
151. Koch E, Walther J, Cuevas M (2009) *Sens Actuator A Phys* 156:8–13
152. Walther J, Koch E (2009) *Opt Express* 17:19698–19713
153. Fujimoto JG (2003) *Nat Biotechnol* 21:1361–1367
154. Pan Y, Farkas DL (1998) *J Biomed Opt* 3:446–455
155. Feldchtein F, Gelikonov V, Iksanov R, Gelikonov G, Kuranov R, Sergeev A, Gladkova N, Ourutina M, Reitze D, Warren J (1998) *Opt Express* 3:239–250
156. Pircher M, Götzinger E, Leitgeb R, Fercher AF, Hitzenberger C (2003) *J Biomed Opt* 8:565–569
157. Schmitt JM, Xiang SH, Yung KM (1998) *J Opt Soc Am A* 15:2288–2296
158. Pircher M, Götzinger E, Leitgeb R, Fercher A, Hitzenberger C (2003) *Opt Express* 11:2190–2197
159. Sacchet D, Moreau J, Georges P, Dubois A (2008) *Opt Express* 16:19434–19446
160. Kray S, Spöler F, Först M, Kurz H (2009) *Opt Lett* 34:1970–1972
161. Adler D, Ko T, Herz P, Fujimoto J (2004) *Opt Express* 12:5487–5501
162. Dubois A, Moreau J, Boccara C (2008) *Opt Express* 16:17082–17091
163. Desjardins AE, Vakoc BJ, Tearney GJ, Bouma BE (2007) *Opt Lett* 32:3158–3160
164. Xu C, Carney P, Boppart S (2005) *Opt Express* 13:5450–5462
165. Faber DJ, Mik EG, Aalders MCG, van Leeuwen TG (2003) *Opt Lett* 28:1436–1438
166. Faber DJ, Mik EG, Aalders MCG, van Leeuwen TG (2005) *Opt Lett* 30:1015–1017
167. Lu CW, Lee CK, Tsai MT, Wang YM, Yang CC (2008) *Opt Lett* 33:416–418
168. Yi J, Li X (2010) *Opt Lett* 35:2094–2096
169. Drexler W (2004) *J Biomed Opt* 9:47–74
170. Kagemann L, Wollstein G, Wojtkowski M, Ishikawa H, Townsend KA, Gabriele ML, Srinivasan VJ, Fujimoto JG, Schuman JS (2007) *J Biomed Opt* 12:041212
171. Liu X, Kang JU (2010) *IEEE Trans Biomed Eng* 57:2572–2575
172. Yang C (2005) *Photochem Photobiol* 81:215–237
173. Xu C, Ye J, Marks DL, Boppart SA (2004) *Opt Lett* 29:1647–1649
174. Yang C, McGuckin LEL, Simon JD, Choma MA, Applegate B, Izatt JA (2004) *Opt Lett* 29:2016–2018
175. Yi J, Gong J, Li X (2009) *Opt Express* 17:13157–13167
176. Kartakoullis A, Bousi E, Pitris C (2010) *Opt Express* 18:9181–9191
177. de Boer JF, Milner TE, van Gemert MJC, Nelson JS (1997) *Opt Lett* 22:934–936
178. Hee MR, Huang D, Swanson EA, Fujimoto JG (1992) *J Opt Soc Am B* 9:903–908
179. Hitzenberger C, Goetzinger E, Sticker M, Pircher M, Fercher A (2001) *Opt Express* 9:780–790
180. Yao G, Wang LV (1999) *Opt Lett* 24:537–539
181. Götzinger E, Pircher M, Hitzenberger CK (2005) *Opt Express* 13:10217–10229
182. Götzinger E, Baumann B, Pircher M, Hitzenberger CK (2009) *Opt Express* 17:22704–22717
183. Al-Qaisi MK, Akkin T (2010) *Opt Express* 18:3392–3403
184. Oh WY, Yun SH, Vakoc BJ, Shishkov M, Desjardins AE, Park BH, de Boer JF, Tearney GJ, Bouma BE (2008) *Opt Express* 16:1096–1103
185. Wang H, Al-Qaisi MK, Akkin T (2010) *Opt Lett* 35:154–156
186. Yamanari M, Makita S, Yasuno Y (2008) *Opt Express* 16:5892–5906
187. Sakai S, Yamanari M, Miyazawa A, Matsumoto M, Nakagawa N, Sugawara T, Kawabata K, Yatagai T, Yasuno Y (2008) *J Invest Dermatol* 128:1641–1647
188. Sakai S, Nakagawa N, Yamanari M, Miyazawa A, Yasuno Y, Matsumoto M (2009) *J Biomed Opt* 14:044032
189. Strasswimmer J, Pierce MC, Park BH, Neel V, de Boer JF (2004) *J Biomed Opt* 9:292–298
190. Bagnaninchi PO, Yang Y, Bonesi M, Maffulli G, Phelan C, Meglinski I, El Haj A, Maffulli N (2010) *Phys Med Biol* 55:3777
191. Nadkarni SK, Pierce MC, Park BH, de Boer JF, Whittaker P, Bouma BE, Bressner JE, Halpern E, Houser SL, Tearney GJ (2007) *J Am Coll Cardiol* 49:1474–1481
192. Kim KH, Burns JA, Bernstein JJ, Maguluri GN, Park BH, de Boer JF (2010) *Opt Express* 18:14644–14653
193. Fanjul-Velez F, Pircher M, Baumann B, Götzinger E, Hitzenberger CK, Arce-Diego JL (2010) *J Biomed Opt* 15:056004
194. Ahlers C, Götzinger E, Pircher M, Golbaz I, Prager F, Schütze C, Baumann B, Hitzenberger CK, Schmidt-Erfurth U (2010) *Invest Ophthalmol Vis Sci* 51:2149–2157
195. Götzinger E, Pircher M, Geitzenauer W, Ahlers C, Baumann B, Michels S, Schmidt-Erfurth U, Hitzenberger CK (2008) *Opt Express* 16:16410–16422
196. Baumann B, Götzinger E, Pircher M, Sattmann H, Schütze C, Schlanitz F, Ahlers C, Schmidt-Erfurth U, Hitzenberger CK (2010) *J Biomed Opt* 15:061704–061709
197. Kim KH, Park BH, Tu Y, Hasan T, Lee B, Li J, de Boer JF (2011) *Opt Express* 19:552–561
198. Beaurepaire E, Moreaux L, Amblard F, Mertz J (1999) *Opt Lett* 24:969–971
199. Yazdanfar S, Chen YY, So PTC, Laiho LH (2007) *Microsc Res Tech* 70:628–633
200. Yuan S, Roney CA, Wierwille J, Chen CW, Xu B, Griffiths G, Jiang J, Ma H, Cable A, Summers RM, Chen Y (2010) *Phys Med Biol* 55:191–206
201. Hoffmann C, Hofer B, Unterhuber A, Poavzay B, Morgner U, Drexler W (2011) In: Azar FS, Intes X (eds) *SPIE, San Francisco, USA*, 78920B
202. Bradu A, Ma L, Bloor JW, Podoleanu A (2009) *J Biophotonics* 2:380–388
203. Rosen RB, Hathaway M, Rogers J, Pedro J, Garcia P, Dobre GM, Podoleanu AG (2009) *Invest Ophthalmol Vis Sci* 50:851–860
204. Helb HM, Issa PC, Fleckenstein M, Schmitz-Valckenberg S, Scholl HPN, Meyer CH, Eter N, Holz FG (2009) *Acta Ophthalmol*

205. Issa PC, Fleckenstein M, Helb HM, Scholl HPN, Schmitz-Valckenberg S, Holz FG (2010) Simultaneous SD-OCT and Confocal SLO-Imaging. In: Medical retina. Springer, Berlin Heidelberg
206. Pan YT, Xie TQ, Du CW, Bastacky S, Meyers S, Zeidel ML (2003) Opt Lett 28:2485–2487
207. Wang ZG, Durand DB, Schoenberg M, Pan YT (2005) J Urol 174:2376–2381
208. Schmidbauer J, Remzi M, Klatte T, Waldert M, Mauermann J, Susani M, Marberger M (2009) Eur Urol 56:914–919
209. Jo JA, Applegate BE, Park J, Shrestha S, Pande P, Gimenez-Conti IB, Brandon JL (2010) IEEE Trans Biomed Eng 57:2596–2599
210. Liang X, Graf BW, Boppart SA (2009) J Biophotonics 2:643–655
211. Tan W, Vinegoni C, Norman JJ, Desai TA, Boppart SA (2007) Microsc Res Tech 70:361–371
212. Vinegoni C, Ralston T, Tan W, Luo W, Marks DL, Boppart SA (2006) Appl Phys Lett 88:053901
213. Joo C, Kim KH, de Boer JF (2007) Opt Lett 32:623–625
214. Wojtkowski M (2010) Appl Opt 49:D30–D61
215. Jiang Y, Tomov I, Wang Y, Chen Z (2004) Opt Lett 29:1090–1092
216. Lee TM, Oldenburg AL, Sitafalwalla S, Marks DL, Luo W, Touban FJ-J, Suslick KS, Boppart SA (2003) Opt Lett 28:1546–1548
217. Oldenburg A, Touban F, Suslick K, Wei A, Boppart S (2005) Opt Express 13:6597–6614